

## Article

# Second-Order Collocation-Based Mixed FEM for Flexoelectric Solids

Kevin Tannhäuser, Prince Henry Serrao  and Sergey Kozinov \* 

Chair of Continuum Mechanics, Ruhr-University Bochum, 44801 Bochum, Germany

\* Correspondence: sergey.kozinov@rub.de

**Abstract:** Flexoelectricity is an electromechanical coupling between the electric field and the mechanical strain gradient, as well as between the mechanical strains and the electric field gradient, observed in all dielectric materials, including those with centrosymmetry. Flexoelectricity demands  $C^1$ -continuity for straightforward numerical implementation as the governing equations in the gradient theory are fourth-order partial differential equations. In this work, an alternative collocation-based mixed finite element method for direct flexoelectricity is used, for which a newly developed quadratic element with a high capability of capturing gradients is introduced. In the collocation method, mechanical strains and electric field through independently assumed polynomials are collocated with the mechanical strains and electric field derived from the mechanical displacements and electric potential at collocation points inside a finite element. The mechanical strain gradient and electric field are obtained by taking the directional derivative of the independent mechanical strain and electric field gradients. However, an earlier proposed linear element is unable to capture all mechanical strain gradient components and, thus, simulate flexoelectricity correctly. This problem is solved in the present work by using quadratic shape functions for the mechanical displacements and electric potential with fewer degrees of freedom than the traditional mixed finite element method. A Fortran user-element code is developed by the authors: first, for the linear and, after that, for the quadratic element. After verifying the linear element with numerical results from the literature, both linear and quadratic elements' behaviors are tested for different problems. It is shown that the proposed second-order collocation-based mixed FEM can capture the flexoelectric behavior better compared to the existing linear formulations.

**Keywords:** flexoelectricity; mixed finite element method; collocation method; biquadratic elements



**Citation:** Tannhäuser, K.; Serrao, P. H.; Kozinov, S. Second-Order Collocation-Based Mixed FEM for Flexoelectric Solids. *Solids* **2023**, *4*, 39–70. <https://doi.org/10.3390/solids4010004>

Academic Editors: Niklas Wolff and Lorenz Kienle

Received: 22 December 2022

Revised: 30 January 2023

Accepted: 31 January 2023

Published: 2 February 2023



**Copyright:** © 2023 by the authors. Licensee MDPI, Basel, Switzerland. This article is an open access article distributed under the terms and conditions of the Creative Commons Attribution (CC BY) license (<https://creativecommons.org/licenses/by/4.0/>).

## 1. Introduction

With the theoretical identification of the flexoelectric effect by Mashkevich and Tolpygo in 1957 [1] and the quantification of flexoelectric coefficients by Kogan in 1964 [2], a new chapter in the research on microelectromechanical systems (MEMS) began. Like other electromechanical effects, such as piezoelectricity, this opened the possibility of constructing new types of sensors and actuators or energy-harvesting devices. Unlike piezoelectricity, which only occurs in noncentrosymmetric crystals, flexoelectricity breaks the inversion symmetry of the crystal structure by inducing mechanical strain gradients. Therefore, flexoelectricity is observed in all dielectrics and is a universal electromechanical effect [3]. This property makes flexoelectricity particularly relevant for materials with high dielectric parameters, such as ferroelectrics [4,5].

Flexoelectricity can be subdivided into direct and converse flexoelectric effects. The first describes the generation of an electric field due to mechanical strain gradients, whereas the converse effect defines the coupling between the electric field gradients and mechanical strains. Typically, the flexoelectric coefficients have small values. High mechanical strain gradients must be induced for flexoelectricity to become a dominant effect. Because flexoelectricity is inversely related to the length scale, this is more easily accomplished

in micro- and nanostructures. Due to the ongoing miniaturization in microelectronics, size-dependent effects play an increasingly important role, making flexoelectricity an essential topic in recent years. Various experiments including cantilever beam and truncated pyramid setups [6–9] have been conducted to quantify flexoelectricity. In order to utilize the flexoelectric effect in electronic devices, analytical formulations have been developed, e.g., for flexoelectricity in one-dimensional nanosized cantilever beams. Based on the theory developed in [10], the formulations for a Bernoulli–Euler beam are derived, in which piezoelectricity and direct flexoelectricity are considered [11]. However, with more complex structures involved, the problems become very difficult to solve analytically. Therefore, different numerical methods were developed to solve this issue. The most popular one is the conventional finite element method (FEM); however, it is not directly suitable for simulating flexoelectricity because of the requirement of  $C^0$ -continuous elements. Consequently, mesh-free formulation [12], isogeometric analysis [13,14], moving least square [15], the hierarchical B-spline method [16], and mixed FEM have been developed to simulate flexoelectricity. For the latter method, numerical results for the “plate with a hole” problem [17,18] and the “infinite length tube” problem [19] were obtained. Furthermore, recently in [20], numerically robust mixed finite elements were proposed for modeling size-dependent flexoelectric behavior in piezoelectric solids to highlight mutual interactions of piezoelectricity and flexoelectricity. It is also possible to use  $C^1$ -continuous elements with higher-order shape functions and additional degrees of freedom (DOFs) as given in [18].

If choosing mixed FEM for flexoelectric behavior simulation, the constraints between the mechanical displacement field and its gradient are enforced by Lagrange multipliers [17]. These Lagrange multipliers are set as extra DOFs. For a 2D quadrilateral element, 27 DOFs are used for mechanical displacements and electric potential on all nine nodes, 16 DOFs are needed for displacement gradients at corner nodes and four Lagrange multipliers are involved at the center node [19]. With this high number of DOFs involved, the stiffness matrix, which has to be inverted to solve the numerical problem, becomes weighty, leading to a low computational efficiency for this element. Furthermore, the standard mixed/hybrid FEM has some drawbacks, like the requirement to satisfy the Ladyzhenskaya–Babuška–Brezzi condition [21] which is, however, not possible a priori.

In the present work, the collocation-based mixed FEM is used. In this method, the mechanical strains derived from the nodal displacements are collocated with independently estimated mechanical strains assumed to be a polynomial. The collocation is done on specific points inside the finite element. These points should be located at the Gaussian points, as pointed out in [22]. The collocation-based mixed FEM was extended for the collocation of an electric and magnetic contribution reducing the sensitivity to mesh distortion and aspect ratio compared to the displacement-based elements [23]. Ref. [24] extended the collocation method for higher-order and 3D elements. A collocation mixed FEM to simulate flexoelectric behavior was developed in [25]. It uses  $C^0$ -continuity and is capable of accounting for the size effect of the mechanical strain gradients. The mechanical strain gradients are thereby obtained by taking the directional derivatives of the independently assumed mechanical strains. This linear collocation-based element only has 12 DOFs corresponding to two mechanical displacements and one electric potential DOF at each node of a four-noded element. Ref. [26] was recently extended for the simulation of semiconductors.

In the proposed manuscript, the collocation-based mixed FEM [25] is further extended, introducing biquadratic elements. For this, independent mechanical strains and the electric field are assumed as a quadratic polynomial. This increases the number of DOFs to 27. However, there are fewer DOFs involved than in traditional mixed FEM [17,19,27]. In the current work, a Fortran user element (UEL) for ABAQUS is developed from scratch to simulate flexoelectricity by using linear and quadratic elements. First, the linear element is verified by comparing the results given in [25] with the results of the linear element developed by the authors, for which few specific mechanical strain gradient components are neglected. Later, the performance of the newly developed quadratic element was

compared to the linear element and studied in detail. The numerical examples presented in our study are both the cantilever beam and the truncated pyramid problems.

The paper is organized as follows: Section 2 introduces the governing equations for flexoelectric material behavior. Sections 3.1 and 3.2 present the collocation mixed FEM formulations for the linear element and introduces the quadratic element by outlining the new developments in the collocation method. Section 4.1 presents the result in which the cantilever beam is used as a numerical example. There, in Section 4.1.1 the validation of the results of the developed linear UEL with the numerical results obtained in [25] is shown. The newly developed quadratic element is validated in Section 4.1.2 by neglecting specific mechanical strain gradient components and comparing the obtained results with the results of the linear element for the cantilever beam problem. Additionally, a convergence of linear and quadratic elements are studied in Section 4.1.3. By comparing the linear and the quadratic element in Section 4.1.4, considerable differences in the results are observed and analyzed. Furthermore, in Section 4.1.5, the material behavior for both element types is investigated for a wide range of flexoelectric coefficients. Also in Section 4.1.6, possibilities for further improvements in the physical correctness of the obtained result for the quadratic element are discussed. In Section 4.2, the numerical results for the truncated pyramid are presented, in which the difference in the electric response is outlined. The final conclusions and discussion are presented in Section 5.

## 2. Flexoelectricity: Constitutive and Governing Equations

The internal energy density  $U$ , which accounts for flexoelectricity [10], can be summarized as

$$U = \frac{1}{2}c_{ijkl}\varepsilon_{ij}\varepsilon_{kl} - \frac{1}{2}a_{ij}E_iE_j - e_{kij}\varepsilon_{ij}E_k + \frac{1}{2}g_{ijklmn}\eta_{kji}\eta_{nml} - f_{ijkl}E_i\eta_{lkj} - b_{ijkl}\varepsilon_{ij}E_{k,l} - \frac{1}{2}h_{ijkl}E_{i,j}E_{k,l}, \quad (1)$$

where  $c_{ijkl}$  and  $a_{ij}$  are the components of the elastic and dielectric permittivity tensors, respectively,  $e_{kij}$  are the components of the piezoelectric tensor,  $f_{ijkl}$  and  $b_{klij}$  are the component of the direct and converse flexoelectricity tensors, whereas  $g_{ijklmn}$  and  $h_{ijkl}$  are the components of the strain gradient elasticity (SGE) tensor and the higher-order electric field gradient tensor, respectively.

The mechanical strain tensor  $\varepsilon$ , mechanical strain gradient tensor  $\eta$  and the electric field  $E$  are defined as

$$\varepsilon_{ij} = \frac{1}{2}(u_{i,j} + u_{j,i}), \quad (2)$$

$$\eta_{kji} = \eta_{kij} = \varepsilon_{ij,k} = \frac{1}{2}(u_{i,jk} + u_{j,ik}), \quad (3)$$

$$E_i = -\phi_{,i}, \quad (4)$$

where  $u_i$  are the components of the mechanical displacement and  $\phi$  is the electric potential.

From the internal energy density Equation (1) the constitutive equations for stress  $\sigma_{ij}$ , higher-order stress  $\tau_{kji}$ , electric displacement  $D_i$  and higher-order electric displacement  $Q_{ij}$  are obtained as partial derivatives with respect to  $\varepsilon_{ij}$ ,  $\eta_{kji}$ ,  $E_i$  and  $E_{i,j}$ , respectively:

$$\sigma_{ij} = \frac{\partial U}{\partial \varepsilon_{ij}} = c_{ijkl} \varepsilon_{kl} - e_{kij} E_k - b_{ijkl} E_{k,l}, \quad (5a)$$

$$\tau_{kji} = \frac{\partial U}{\partial \eta_{kji}} = g_{ijklmn} \eta_{nml} - f_{lijk} E_l, \quad (5b)$$

$$D_i = -\frac{\partial U}{\partial E_i} = a_{ij} E_j + e_{ijk} \varepsilon_{jk} + f_{ijkl} \eta_{lkj}, \quad (5c)$$

$$Q_{ij} = -\frac{\partial U}{\partial E_{i,j}} = b_{klj} \varepsilon_{kl} + h_{ijkl} E_{k,l}. \quad (5d)$$

In order to account for the size effect of the mechanical strain gradients and electric field gradients, internal length scale parameters  $l$  and  $q$  are introduced. These parameters are multiplied with the elastic stiffness coefficients  $c_{ijkl}$  and the dielectric coefficients  $a_{ij}$  to get the higher-order elastic parameters  $g_{ijklmn}$  and the higher-order electric parameters  $h_{ijkl}$  of Equations (5b) and (5d), respectively [25,28]:

$$g_{ijklmn} = l^2 c_{jkmn} \delta_{il}, \quad (6)$$

$$h_{ijkl} = q^2 a_{ik} \delta_{jl}. \quad (7)$$

Here,  $\delta_{ij}$  denotes the Kronecker delta and  $c_{jkmn}$  and  $a_{ik}$  are given for orthotropic material as

$$a_{ij} = a_1 \delta_{i1} \delta_{j1} + a_3 \delta_{i3} \delta_{j3}, \quad (8)$$

$$c_{ijkl} = \delta_{i1} \delta_{j1} (c_{11} \delta_{k1} \delta_{l1} + c_{13} \delta_{k3} \delta_{l3}) + \delta_{i3} \delta_{j3} (c_{13} \delta_{k1} \delta_{l1} + c_{33} \delta_{k3} \delta_{l3}) + c_{44} (\delta_{i1} \delta_{j3} + \delta_{i3} \delta_{j1}) (\delta_{k1} \delta_{l3} + \delta_{k3} \delta_{l1}). \quad (9)$$

For a 4 mm tetragonal crystal structure, the piezoelectric coefficients  $e_{kij}$  are given by [25,29]

$$e_{kij} = -(e_{31} \delta_{i1} \delta_{j1} + e_{33} \delta_{i3} \delta_{j3}) \delta_{k3} - e_{15} (\delta_{i1} \delta_{j3} + \delta_{i3} \delta_{j1}) \delta_{k1}, \quad (10)$$

where the indices 1 and 3 describe two dimensions of a 2D Cartesian coordinate system in which 3 is the poling direction. So the stress due to piezoelectricity can be written as

$$\sigma_{11} = -e_{31} E_3, \quad \sigma_{33} = -e_{33} E_3, \quad \sigma_{13} = -e_{15} E_1. \quad (11)$$

The direct and converse flexoelectric tensors have low symmetry. For a cubic crystal, they can be expressed by three independent coefficients [30]. For converse flexoelectricity, the coefficients  $b_{klj}$  are represented as  $b_1$ ,  $b_2$  and  $b_3$  [30]:

$$b_{klj} = -\delta_{i1} \delta_{j1} (b_1 \delta_{k1} \delta_{l1} + b_2 \delta_{k3} \delta_{l3}) - \delta_{i3} \delta_{j3} (b_2 \delta_{k1} \delta_{l1} + b_1 \delta_{k3} \delta_{l3}) - b_3 (\delta_{i1} \delta_{j3} + \delta_{i3} \delta_{j1}) (\delta_{k1} \delta_{l3} + \delta_{k3} \delta_{l1}). \quad (12)$$

The stress due to converse flexoelectricity can be written as

$$\sigma_{11} = -b_1 E_{1,1} - b_2 E_{3,3}, \quad (13a)$$

$$\sigma_{33} = -b_2 E_{1,1} - b_1 E_{3,3}, \quad (13b)$$

$$\sigma_{13} = \sigma_{31} = -b_3 (E_{1,3} + E_{3,1}). \quad (13c)$$

For direct flexoelectricity, the coefficients  $f_{ijkl}$  can be reduced further to two independent components  $f_1$  and  $f_2$  when isotropic material is considered [19,30]:

$$f_{ijkl} = f_1 \delta_{ij} \delta_{kl} + f_2 (\delta_{il} \delta_{jk} + \delta_{ik} \delta_{jl}). \quad (14)$$

By applying the Voigt notation, the constitutive Equations (5a)–(5d) can be presented as [25]

$$\begin{bmatrix} \sigma_{11} \\ \sigma_{33} \\ \sigma_{13} \end{bmatrix} = \mathbf{C} \begin{bmatrix} \varepsilon_{11} \\ \varepsilon_{33} \\ 2\varepsilon_{13} \end{bmatrix} - \mathbf{e} \begin{bmatrix} E_1 \\ E_3 \end{bmatrix} - \mathbf{b} [ E_{1,1} \quad E_{3,1} \quad E_{1,3} \quad E_{3,3} ]^T, \tag{15a}$$

$$\begin{bmatrix} D_1 \\ D_3 \end{bmatrix} = \mathbf{e}^T \begin{bmatrix} \varepsilon_{11} \\ \varepsilon_{33} \\ 2\varepsilon_{13} \end{bmatrix} + \mathbf{a} \begin{bmatrix} E_1 \\ E_3 \end{bmatrix} + \mathbf{F} [ \eta_{111} \quad \eta_{133} \quad 2\eta_{113} \quad \eta_{311} \quad \eta_{333} \quad 2\eta_{313} ]^T, \tag{15b}$$

$$[ \tau_{111} \quad \tau_{133} \quad \tau_{113} \quad \tau_{311} \quad \tau_{333} \quad \tau_{313} ]^T = -\mathbf{F}^T \begin{bmatrix} E_1 \\ E_3 \end{bmatrix} + l^2 \mathbf{G} [ \eta_{111} \quad \eta_{133} \quad 2\eta_{113} \quad \eta_{311} \quad \eta_{333} \quad 2\eta_{313} ]^T, \tag{15c}$$

$$[ Q_{11} \quad Q_{31} \quad Q_{13} \quad Q_{33} ]^T = \mathbf{b}^T \begin{bmatrix} \varepsilon_{11} \\ \varepsilon_{33} \\ 2\varepsilon_{13} \end{bmatrix} + q^2 \mathbf{H} [ E_{1,1} \quad E_{3,1} \quad E_{1,3} \quad E_{3,3} ]^T, \tag{15d}$$

with material tensors from Equations (6)–(10), (12) and (14) written as matrices  $\mathbf{G}$ ,  $\mathbf{H}$ ,  $\mathbf{a}$ ,  $\mathbf{C}$ ,  $\mathbf{e}$ ,  $\mathbf{b}$ ,  $\mathbf{F}$ , respectively:

$$\begin{aligned} \mathbf{C} &= \begin{bmatrix} c_{11} & c_{13} & 0 \\ c_{13} & c_{33} & 0 \\ 0 & 0 & c_{44} \end{bmatrix}, \quad \mathbf{e} = \begin{bmatrix} 0 & e_{31} \\ 0 & e_{33} \\ e_{15} & 0 \end{bmatrix}, \quad \mathbf{a} = \begin{bmatrix} a_1 & 0 \\ 0 & a_3 \end{bmatrix}, \\ \mathbf{F} &= \begin{bmatrix} f_1 + 2f_2 & f_1 & 0 & 0 & 0 & f_2 \\ 0 & 0 & f_2 & f_1 & f_1 + 2f_2 & 0 \end{bmatrix}, \quad \mathbf{b} = \begin{bmatrix} b_1 & 0 & 0 & b_2 \\ b_2 & 0 & 0 & b_1 \\ 0 & b_3 & b_3 & 0 \end{bmatrix}, \tag{16} \\ \mathbf{G} &= \begin{bmatrix} c_{11} & c_{13} & 0 & 0 & 0 & 0 \\ c_{13} & c_{33} & 0 & 0 & 0 & 0 \\ 0 & 0 & c_{44} & 0 & 0 & 0 \\ 0 & 0 & 0 & c_{11} & c_{13} & 0 \\ 0 & 0 & 0 & c_{13} & c_{33} & 0 \\ 0 & 0 & 0 & 0 & 0 & c_{44} \end{bmatrix}, \quad \mathbf{H} = \begin{bmatrix} a_1 & 0 & 0 & 0 \\ 0 & a_2 & 0 & 0 \\ 0 & 0 & a_1 & 0 \\ 0 & 0 & 0 & a_2 \end{bmatrix}. \end{aligned}$$

The governing equations for a piezoelectric solid with direct and converse flexoelectric effects in the absence of the body forces and free charges can be written as [18,25]

$$\sigma_{ij,j} - \tau_{ijk,jk} = 0, \tag{17a}$$

$$D_{i,i} - Q_{ij,ji} = 0. \tag{17b}$$

The Dirichlet boundary conditions are prescribed as

$$u_i = \bar{u}_i \quad \text{on} \quad \Gamma_u, \tag{18a}$$

$$w_i = \frac{\partial u_i}{\partial n} = \bar{w}_i \quad \text{on} \quad \Gamma_w, \tag{18b}$$

$$\phi = \bar{\phi} \quad \text{on} \quad \Gamma_\phi, \tag{18c}$$

$$p = \frac{\partial \phi}{\partial n} = \bar{p}_i \quad \text{on} \quad \Gamma_p \tag{18d}$$

on the boundary  $\Gamma$  with normal derivative of mechanical displacement  $w_i$  and normal derivative of electric potential  $p$ .  $\Gamma_u, \Gamma_w, \Gamma_\phi$  and  $\Gamma_p$  describe mechanical displacement boundary, boundary of normal derivative of mechanical displacement, electrical potential bound-

ary, and boundary of normal derivative of electric potential, respectively. The bar over the variables indicates that it is a prescribed value. The Neumann boundary conditions are

$$t_i = \bar{t}_i \quad \text{on} \quad \Gamma_t, \quad (19a)$$

$$R_i = n_k n_j \tau_{ijk} = \bar{R}_i \quad \text{on} \quad \Gamma_R, \quad (19b)$$

$$S = \bar{S} \quad \text{on} \quad \Gamma_S, \quad (19c)$$

$$Z = n_i n_j Q_{ij} = \bar{Z} \quad \text{on} \quad \Gamma_Z, \quad (19d)$$

where  $R_i$  denotes the higher-order traction and  $Z$  is the higher-order surface charge. Traction boundary, higher-order traction boundary, electrical surface charge boundary and higher-order surface charge boundary are denoted as  $\Gamma_t$ ,  $\Gamma_R$ ,  $\Gamma_S$  and  $\Gamma_Z$ , respectively:

$$\Gamma_t \cup \Gamma_u = \Gamma, \quad \Gamma_t \cap \Gamma_u = \emptyset, \quad (20a)$$

$$\Gamma_R \cup \Gamma_w = \Gamma, \quad \Gamma_R \cap \Gamma_w = \emptyset, \quad (20b)$$

$$\Gamma_S \cup \Gamma_\phi = \Gamma, \quad \Gamma_S \cap \Gamma_\phi = \emptyset, \quad (20c)$$

$$\Gamma_Z \cup \Gamma_p = \Gamma, \quad \Gamma_Z \cap \Gamma_p = \emptyset. \quad (20d)$$

The traction vector  $t_i$  and the electrical surface charge  $S$  are defined as [25]

$$t_i = n_j \left( \sigma_{ij} - \tau_{ijk,k} \right) - \frac{\partial \rho_i}{\partial \pi} + \sum_k \|\rho_i(\mathbf{x}_k)\| \delta(\mathbf{x} - \mathbf{x}_k), \quad (21a)$$

$$S = n_k \left( D_k - Q_{kj,j} \right) - \frac{\partial \alpha}{\partial \pi} + \sum_k \|\alpha(\mathbf{x}_k)\| \delta(\mathbf{x} - \mathbf{x}_k), \quad (21b)$$

where  $\rho_i = n_k \pi_j \tau_{ijk}$  and  $\alpha = n_i \pi_j Q_{ij}$ .  $\pi_i$  describes the Cartesian component of the unit tangent vector on boundary  $\Gamma$ , and  $\delta(\mathbf{x})$  is the Dirac delta function.  $\|\rho_i(\mathbf{x}_k)\|$  and  $\|\alpha(\mathbf{x}_k)\|$  mean the jump at a corner  $\mathbf{x}_k$  on the oriented boundary contour  $\Gamma$ .

### 3. Collocation Mixed Finite Element Method (CMFEM)

For the numerical simulation of the direct and converse flexoelectricity, one needs to calculate mechanical strains, mechanical strain gradients, electric field, and electric field gradients. As mechanical strain gradients and electric field gradients are the second derivatives of mechanical displacement and electric potential, respectively,  $C^1$ -continuity is required in traditional FEM. To avoid  $C^1$ -continuous elements due to their complexity, mixed FEM is traditionally used for simulating flexoelectricity [17,19,27]. To reduce the number of DOFs and increase computational efficiency, CMFEM, used in this study, was proposed for flexoelectricity and extensionally developed by [25]. In CMFEM, independently assumed mechanical strains and independently assumed electric field are introduced and collocated with the mechanical strains and electric field computed from the mechanical displacement  $u_i$  and electric potential  $\phi$ .  $u_i$  and  $\phi$  are interpolated from the nodal values  $u_i^a$  and  $\phi^a$  inside the finite element, respectively:

$$\begin{bmatrix} u_1(\mathbf{x}) \\ u_3(\mathbf{x}) \end{bmatrix} = \sum_{a=1}^n N^a(\mathbf{r}) \begin{bmatrix} u_1^a \\ u_3^a \end{bmatrix} = \sum_{a=1}^n N^a(\mathbf{r}) \mathbf{u}^a, \quad (22)$$

$$\phi(\mathbf{x}) = \sum_{a=1}^n N^a(\mathbf{r}) \phi^a. \quad (23)$$

Here,  $n$  is the total number of nodes and  $\mathbf{r} = [r \ s]^T$  is the position vector in the local curvilinear coordinate system. In order to calculate the gradient in the global coordinate system, the following coordinate transformation equation is needed (Figure 1)

$$\frac{\partial}{\partial \mathbf{x}} = \mathbf{J}^{-1}(\mathbf{r}) \frac{\partial}{\partial \mathbf{r}'}$$

$$\begin{bmatrix} \frac{\partial}{\partial x_1} \\ \frac{\partial}{\partial x_2} \\ \frac{\partial}{\partial x_3} \end{bmatrix} = \begin{bmatrix} j_{11}^{inv} & j_{13}^{inv} \\ j_{31}^{inv} & j_{33}^{inv} \end{bmatrix} \begin{bmatrix} \frac{\partial}{\partial r} \\ \frac{\partial}{\partial s} \end{bmatrix}. \quad (24)$$

Therefore, the Jacobian matrix  $\mathbf{J}$  in Equation (24) is calculated with the derivatives of the shape functions  $N^a$  and the coordinates of each node  $x_i^a$ . We have

$$\mathbf{J}(\mathbf{r}) = \sum_{a=1}^n \begin{bmatrix} \frac{\partial N^a(\mathbf{r})}{\partial r} x_1^a & \frac{\partial N^a(\mathbf{r})}{\partial s} x_3^a \\ \frac{\partial N^a(\mathbf{r})}{\partial s} x_1^a & \frac{\partial N^a(\mathbf{r})}{\partial s} x_3^a \end{bmatrix}. \quad (25)$$

The global derivative of shape function  $N^a$  with respect to  $x_1$  and  $x_3$  are introduced as  $b_1^a$  and  $b_3^a$ , respectively, by multiplying Equation (24) with shape functions  $N^a$ :

$$\begin{bmatrix} b_1^a(\mathbf{r}) \\ b_3^a(\mathbf{r}) \end{bmatrix} = \begin{bmatrix} j_{11}^{inv} \frac{\partial N^a(\mathbf{r})}{\partial r} + j_{13}^{inv} \frac{\partial N^a(\mathbf{r})}{\partial s} \\ j_{31}^{inv} \frac{\partial N^a(\mathbf{r})}{\partial r} + j_{33}^{inv} \frac{\partial N^a(\mathbf{r})}{\partial s} \end{bmatrix}. \quad (26)$$

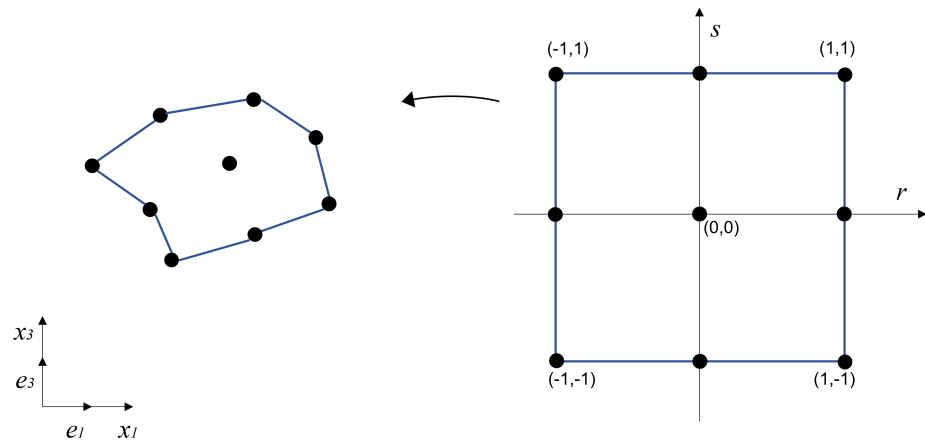


**Figure 1.** General two-dimensional coordinate transformation of a quadrilateral element from local curvilinear coordinates to a global Cartesian coordinate system.

The mechanical strains and electric field are derived from the mechanical displacements and the electric potential, respectively,

$$\boldsymbol{\varepsilon}(\mathbf{x}) = \begin{bmatrix} \varepsilon_{11}(\mathbf{x}) \\ \varepsilon_{33}(\mathbf{x}) \\ 2\varepsilon_{13}(\mathbf{x}) \end{bmatrix} = \sum_{a=1}^N \begin{bmatrix} \mathbf{B}_{\varepsilon_{11}}^{a,T}(\mathbf{r}) \\ \mathbf{B}_{\varepsilon_{33}}^{a,T}(\mathbf{r}) \\ \mathbf{B}_{\varepsilon_{13}}^{a,T}(\mathbf{r}) \end{bmatrix} \mathbf{u}_i^a, \quad (27)$$

$$-\mathbf{E}(\mathbf{x}) = - \begin{bmatrix} E_1(\mathbf{x}) \\ E_3(\mathbf{x}) \end{bmatrix} = \begin{bmatrix} \phi_{,1}(\mathbf{x}) \\ \phi_{,3}(\mathbf{x}) \end{bmatrix} = \sum_{a=1}^N \begin{bmatrix} b_1^a(\mathbf{r}) \\ b_3^a(\mathbf{r}) \end{bmatrix} \phi^a. \quad (28)$$

Here,  $\mathbf{B}_{\varepsilon_{11}}^{a,T}(\mathbf{r})$ ,  $\mathbf{B}_{\varepsilon_{33}}^{a,T}(\mathbf{r})$  and  $\mathbf{B}_{\varepsilon_{13}}^{a,T}(\mathbf{r})$  are the strain-displacement connectivity matrix components

$$\mathbf{B}_{\varepsilon_{11}}^{a,T}(\mathbf{r}) = [ b_1^a(\mathbf{r}) \ 0 ], \quad \mathbf{B}_{\varepsilon_{33}}^{a,T}(\mathbf{r}) = [ 0 \ b_3^a(\mathbf{r}) ], \quad \mathbf{B}_{\varepsilon_{13}}^{a,T}(\mathbf{r}) = [ b_3^a(\mathbf{r}) \ b_1^a(\mathbf{r}) ]. \quad (29)$$

### 3.1. CMFEM for Linear Element

The idea of the collocation method is that a polynomial is assumed for each component of the independent mechanical strain and electric field. These polynomials consist of a  $\mathbf{P}$ -vector and a coefficient vector  $\boldsymbol{\beta}$  or  $\boldsymbol{\alpha}$

$$\boldsymbol{\varepsilon}_{ii}^{\text{In}} = \mathbf{P}^T(\mathbf{r})\boldsymbol{\alpha}_{ii}, \quad 2\boldsymbol{\varepsilon}_{13}^{\text{In}} = \mathbf{P}^T(\mathbf{r})\boldsymbol{\alpha}_{13}, \quad (30)$$

$$-E_i^{\text{In}} = \mathbf{P}^T(\mathbf{r})\boldsymbol{\beta}_i. \quad (31)$$

Here, the superscript "In" describes an independent quantity. The shape of the  $\mathbf{P}$ -vector and the coefficient vector depends on whether the collocated, independent component is assumed to be constant, linear, or quadratic. For the linear element, all components of mechanical strain and electric field are collocated linearly. Consequently, the independent  $\mathbf{P}$ -vector is defined as follows:

$$\mathbf{P}(\mathbf{r}) = [1 \quad r \quad s \quad rs]. \quad (32)$$

The corresponding coefficient vectors have to be assumed accordingly, so that the number of components is the same as for the assumed  $\mathbf{P}$  vector

$$\boldsymbol{\alpha}_{11} = [1\alpha \quad 2\alpha \quad 3\alpha \quad 4\alpha]^T, \quad (33a)$$

$$\boldsymbol{\alpha}_{33} = [5\alpha \quad 6\alpha \quad 7\alpha \quad 8\alpha]^T, \quad (33b)$$

$$\boldsymbol{\alpha}_{13} = [9\alpha \quad 10\alpha \quad 11\alpha \quad 12\alpha]^T, \quad (33c)$$

$$\boldsymbol{\beta}_1 = [1\beta \quad 2\beta \quad 3\beta \quad 4\beta]^T, \quad (33d)$$

$$\boldsymbol{\beta}_3 = [5\beta \quad 6\beta \quad 7\beta \quad 8\beta]^T. \quad (33e)$$

The left top indices distinguish different coefficients. Because the coefficients  ${}^i\alpha$  and  ${}^i\beta$  for the assumed polynomials are not known initially, these have to be computed by using the collocation method. For this, the quantities which are derived from nodal values are set to be equal to the independently assumed quantities at collocation points  $\mathbf{x}_c$ . The collocation points must be at specific positions inside the finite element, which have to be the Gaussian points to pass the patch test [22,23]. Consequently,  $\varepsilon_{ij}$  and  $E_i$  are collocated at the  $2 \times 2$  Gaussian points 5, 6, 7, and 8 in Figure 2.

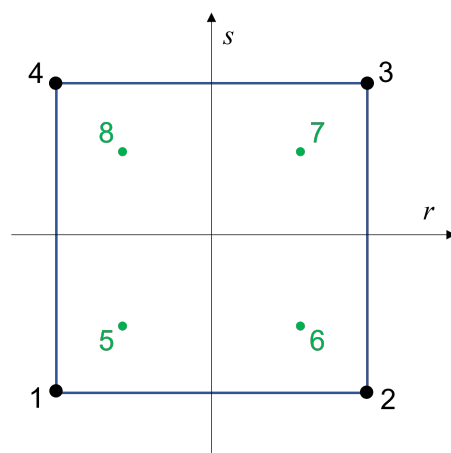


**Figure 2.** Four-noded quadrilateral element in the local curvilinear coordinate system with  $2 \times 2$  Gaussian quadrature points.

We have

$$\varepsilon_{ii}^{\text{In}}(\mathbf{x}_c) = \varepsilon_{ii}(\mathbf{x}_c), \quad 2\varepsilon_{13}^{\text{In}}(\mathbf{x}_c) = 2\varepsilon_{13}(\mathbf{x}_c), \quad E_i^{\text{In}}(\mathbf{x}_c) = E_i(\mathbf{x}_c). \quad (34)$$

By assembling  $\mathbf{P}$ -vectors for all collocation points,  $\mathbf{A}$  matrix is obtained.  $\mathbf{A}$  contains the coordinates of all considered collocation points, and hence can be precalculated for each Gaussian point as

$$\mathbf{A}\boldsymbol{\alpha}_{ij} = \sum_{a=1}^n \mathbf{B}_{ij}^a(\mathbf{r}_c) \mathbf{u}^a, \quad (35)$$

$$\mathbf{A}\boldsymbol{\beta}_i = \sum_{a=1}^n \mathbf{B}_{Ei}^a(\mathbf{r}_c) \phi^a, \quad (36)$$

where

$$\mathbf{A} = \begin{bmatrix} 1 & r_5 & s_5 & r_5 s_5 \\ 1 & r_6 & s_6 & r_6 s_6 \\ 1 & r_7 & s_7 & r_7 s_7 \\ 1 & r_8 & s_8 & r_8 s_8 \end{bmatrix}. \quad (37)$$

The subscript of  $r$  and  $s$  denotes the collocation points. The  $\mathbf{B}^a$ -matrices in Equations (35) and (36) can be written as follows:

$$\mathbf{B}_{\varepsilon_{11}}^{a,T}(\mathbf{r}_c) = \begin{bmatrix} b_1^a(\mathbf{r}_5) & b_1^a(\mathbf{r}_6) & b_1^a(\mathbf{r}_7) & b_1^a(\mathbf{r}_8) \\ 0 & 0 & 0 & 0 \end{bmatrix}, \quad \mathbf{B}_{\varepsilon_{33}}^{a,T}(\mathbf{r}_c) = \begin{bmatrix} 0 & 0 & 0 & 0 \\ b_3^a(\mathbf{r}_5) & b_3^a(\mathbf{r}_6) & b_3^a(\mathbf{r}_7) & b_3^a(\mathbf{r}_8) \end{bmatrix}, \quad (38a)$$

$$\mathbf{B}_{\varepsilon_{13}}^{a,T}(\mathbf{r}_c) = \begin{bmatrix} b_3^a(\mathbf{r}_5) & b_3^a(\mathbf{r}_6) & b_3^a(\mathbf{r}_7) & b_3^a(\mathbf{r}_8) \\ b_1^a(\mathbf{r}_5) & b_1^a(\mathbf{r}_6) & b_1^a(\mathbf{r}_7) & b_1^a(\mathbf{r}_8) \end{bmatrix}, \quad \mathbf{B}_{Ei}^{a,T}(\mathbf{r}_c) = \begin{bmatrix} b_i^a(\mathbf{r}_5) & b_i^a(\mathbf{r}_6) & b_i^a(\mathbf{r}_7) & b_i^a(\mathbf{r}_8) \end{bmatrix}. \quad (38b)$$

From Equations (35) and (36) the coefficient vectors are obtained and inserted into Equations (30) and (31) as

$$\boldsymbol{\varepsilon}^{\text{In}}(\mathbf{x}) = \begin{bmatrix} \varepsilon_{11}^{\text{In}}(\mathbf{x}) \\ \varepsilon_{33}^{\text{In}}(\mathbf{x}) \\ 2\varepsilon_{13}^{\text{In}}(\mathbf{x}) \end{bmatrix} = \sum_a \mathbf{B}_{\mathbf{u}}^a(\mathbf{r}) \mathbf{u}^a = \mathbf{B}_{\mathbf{u}} \mathbf{u}, \quad (39)$$

$$\mathbf{E}^{\text{In}}(\mathbf{x}) = \begin{bmatrix} E_1^{\text{In}}(\mathbf{x}) \\ E_3^{\text{In}}(\mathbf{x}) \end{bmatrix} = \sum_a \mathbf{B}_{\phi}^a(\mathbf{r}) \phi^a = \mathbf{B}_{\phi} \boldsymbol{\phi}, \quad (40)$$

where  $\mathbf{u}$  and  $\boldsymbol{\phi}$  contain the mechanical displacement and electric potential for all nodes, respectively, and the newly introduced  $\mathbf{B}_{\mathbf{u}}^a$ - and  $\mathbf{B}_{\phi}^a$ -matrices are being calculated as

$$\mathbf{B}_{\mathbf{u}}^a(\mathbf{r}) = \begin{bmatrix} \mathbf{P}^T(\mathbf{r})\mathbf{A}^{-1}\mathbf{B}_{\varepsilon_{11}}^a(\mathbf{r}_c) \\ \mathbf{P}^T(\mathbf{r})\mathbf{A}^{-1}\mathbf{B}_{\varepsilon_{33}}^a(\mathbf{r}_c) \\ \mathbf{P}^T(\mathbf{r})\mathbf{A}^{-1}\mathbf{B}_{\varepsilon_{13}}^a(\mathbf{r}_c) \end{bmatrix}, \quad \mathbf{B}_{\phi}^a(\mathbf{r}) = \begin{bmatrix} \mathbf{P}^T(\mathbf{r})\mathbf{A}^{-1}\mathbf{B}_{E1}^a(\mathbf{r}_c) \\ \mathbf{P}^T(\mathbf{r})\mathbf{A}^{-1}\mathbf{B}_{E3}^a(\mathbf{r}_c) \end{bmatrix}. \quad (41)$$

By taking the directional derivative of  $\mathbf{P}$ , mechanical strain gradients and electric field gradients are obtained [25] as

$$\frac{\partial \boldsymbol{\varepsilon}^{\text{In}}(\mathbf{x})}{\partial x_i} = \begin{bmatrix} \mathbf{P}_{,i}^T \mathbf{A}^{-1} \mathbf{B}_{\varepsilon_{11}}(\mathbf{r}_c) \\ \mathbf{P}_{,i}^T \mathbf{A}^{-1} \mathbf{B}_{\varepsilon_{33}}(\mathbf{r}_c) \\ \mathbf{P}_{,i}^T \mathbf{A}^{-1} \mathbf{B}_{\varepsilon_{13}}(\mathbf{r}_c) \end{bmatrix} \mathbf{u}, \quad (42)$$

$$\frac{\partial \mathbf{E}^{\text{In}}(\mathbf{x})}{\partial x_i} = \begin{bmatrix} \mathbf{P}_{,i}^T \mathbf{A}^{-1} \mathbf{B}_{E1}(\mathbf{r}_c) \\ \mathbf{P}_{,i}^T \mathbf{A}^{-1} \mathbf{B}_{E3}(\mathbf{r}_c) \end{bmatrix} \boldsymbol{\phi}, \quad (43)$$

where

$$\begin{bmatrix} \mathbf{P}_{,1}^T \\ \mathbf{P}_{,3}^T \end{bmatrix} = \begin{bmatrix} j_{11}^{inv}(\mathbf{r}) & j_{13}^{inv}(\mathbf{r}) \\ j_{31}^{inv}(\mathbf{r}) & j_{33}^{inv}(\mathbf{r}) \end{bmatrix} \begin{bmatrix} \frac{\partial \mathbf{P}^T(\mathbf{r})}{\partial r} \\ \frac{\partial \mathbf{P}^T(\mathbf{r})}{\partial s} \end{bmatrix}. \quad (44)$$

Applying the Voigt notation for the mechanical strain gradients and the electric field gradients, the following equations are obtained:

$$\boldsymbol{\eta}^{In}(\mathbf{x}) = \begin{bmatrix} \mathbf{P}_1^T \mathbf{A}^{-1} \mathbf{B}_{\varepsilon 11}(\mathbf{r}_c) \\ \mathbf{P}_1^T \mathbf{A}^{-1} \mathbf{B}_{\varepsilon 33}(\mathbf{r}_c) \\ \mathbf{P}_1^T \mathbf{A}^{-1} \mathbf{B}_{\varepsilon 13}(\mathbf{r}_c) \\ \mathbf{P}_3^T \mathbf{A}^{-1} \mathbf{B}_{\varepsilon 11}(\mathbf{r}_c) \\ \mathbf{P}_3^T \mathbf{A}^{-1} \mathbf{B}_{\varepsilon 33}(\mathbf{r}_c) \\ \mathbf{P}_3^T \mathbf{A}^{-1} \mathbf{B}_{\varepsilon 13}(\mathbf{r}_c) \end{bmatrix} \mathbf{u} = \mathbf{B}_{\nabla \mathbf{u}} \mathbf{u}, \quad (45)$$

$$-\mathbf{E}^{In}(\mathbf{x}) = \begin{bmatrix} \mathbf{P}_1^T \mathbf{A}^{-1} \mathbf{B}_{E1}(\mathbf{r}_c) \\ \mathbf{P}_1^T \mathbf{A}^{-1} \mathbf{B}_{E3}(\mathbf{r}_c) \\ \mathbf{P}_3^T \mathbf{A}^{-1} \mathbf{B}_{E1}(\mathbf{r}_c) \\ \mathbf{P}_3^T \mathbf{A}^{-1} \mathbf{B}_{E3}(\mathbf{r}_c) \end{bmatrix} \boldsymbol{\phi} = \mathbf{B}_{\nabla \boldsymbol{\phi}} \boldsymbol{\phi}. \quad (46)$$

The variational condition describes the equivalence of the variational internal work and the variational external work. In gradient theory for FEM, it can be derived as [10]

$$\begin{aligned} \int_V (\sigma_{ij} \delta \varepsilon_{ij} + \tau_{kij} \delta \eta_{kij} - D_k \delta E_k - Q_{ij} \delta E_{i,j}) d\Omega &= \int_{\Gamma_t} t_i \delta u_i d\Gamma + \int_{\Gamma_R} R_i \delta w_i \Gamma \\ &+ \int_{\Gamma_S} S \delta \phi \Gamma + \int_{\Gamma_Z} Z \delta p \Gamma. \end{aligned} \quad (47)$$

In order to implement described formulations, the stiffness matrix for the flexoelectric material has to be derived. Therefore, the expressions for mechanical strains, mechanical strain gradients, electric field, and electric field gradients obtained by the collocation method and the constitutive Equations (5a) and (5d) are inserted into the variational condition Equation (47):

$$\begin{aligned} &\sum_e \int_{V_e} \delta \mathbf{u}^T \left( \mathbf{B}_{\mathbf{u}}^T(\mathbf{r}) \mathbf{C} \mathbf{B}_{\mathbf{u}}(\mathbf{r}) + l^2 \mathbf{B}_{\nabla \mathbf{u}}^T(\mathbf{r}) \mathbf{G} \mathbf{B}_{\nabla \mathbf{u}}(\mathbf{r}) \right) \mathbf{u} dV_e \\ &+ \sum_e \int_{V_e} \delta \mathbf{u}^T \left( \mathbf{B}_{\mathbf{u}}^T(\mathbf{r}) \mathbf{e} \mathbf{B}_{\boldsymbol{\phi}}(\mathbf{r}) + \mathbf{B}_{\mathbf{u}}^T(\mathbf{r}) \mathbf{b} \mathbf{B}_{\nabla \boldsymbol{\phi}}(\mathbf{r}) + \mathbf{B}_{\nabla \mathbf{u}}^T(\mathbf{r}) \mathbf{F}^T \mathbf{B}_{\boldsymbol{\phi}}(\mathbf{r}) \right) \boldsymbol{\phi} dV_e \\ &+ \sum_e \int_{V_e} \delta \boldsymbol{\phi}^T \left( \mathbf{B}_{\boldsymbol{\phi}}^T(\mathbf{r}) \mathbf{e}^T \mathbf{B}_{\mathbf{u}}(\mathbf{r}) + \mathbf{B}_{\boldsymbol{\phi}}^T(\mathbf{r}) \mathbf{F} \mathbf{B}_{\nabla \mathbf{u}}(\mathbf{r}) + \mathbf{B}_{\nabla \boldsymbol{\phi}}^T(\mathbf{r}) \mathbf{b}^T \mathbf{B}_{\mathbf{u}}(\mathbf{r}) \right) \mathbf{u} dV_e \\ &- \sum_e \int_{V_e} \delta \boldsymbol{\phi}^T \left( \mathbf{B}_{\boldsymbol{\phi}}^T(\mathbf{r}) \mathbf{a} \mathbf{B}_{\boldsymbol{\phi}}(\mathbf{r}) + q^2 \mathbf{B}_{\nabla \boldsymbol{\phi}}^T(\mathbf{r}) \mathbf{H} \mathbf{B}_{\nabla \boldsymbol{\phi}}(\mathbf{r}) \right) \boldsymbol{\phi} dV_e = \\ &\sum_e \sum_{a=1}^n \delta \mathbf{u}^T \left( \int_{\Gamma_t^e} N^a \bar{\mathbf{t}}^a d\Gamma + \int_{\Gamma_R^e} n_j b_j^a \bar{\mathbf{R}}^a d\Gamma \right) + \delta \boldsymbol{\phi}^T \left( \int_{\Gamma_S^e} N^a \bar{S}^a d\Gamma + \int_{\Gamma_Z^e} n_j b_j^a \bar{Z}^a d\Gamma \right). \end{aligned} \quad (48)$$

Here,  $e$  denotes an element and  $V_e$  the volume of an element.  $\bar{\mathbf{t}}^a$  and  $\bar{\mathbf{R}}^a$  are given as

$$\bar{\mathbf{t}}^a = \begin{bmatrix} \bar{t}_1^a & \bar{t}_3^a \end{bmatrix}^T, \quad (49)$$

$$\bar{\mathbf{R}}^a = \begin{bmatrix} \bar{R}_1^a & \bar{R}_3^a \end{bmatrix}^T, \quad (50)$$

where the superscript is the node number. Because the variation  $\delta \mathbf{u}$  and  $\delta \boldsymbol{\phi}$  can be arbitrary, Equation (48) splits into two equations which can be written for each element as

$$\begin{bmatrix} \mathbf{K}_{\mathbf{u}\mathbf{u}} & \mathbf{K}_{\mathbf{u}\boldsymbol{\phi}} \\ \mathbf{K}_{\boldsymbol{\phi}\mathbf{u}} & \mathbf{K}_{\boldsymbol{\phi}\boldsymbol{\phi}} \end{bmatrix} \begin{bmatrix} \mathbf{u} \\ \boldsymbol{\phi} \end{bmatrix} = \begin{bmatrix} \mathbf{F}_{\mathbf{u}} \\ \mathbf{F}_{\boldsymbol{\phi}} \end{bmatrix} \quad (51)$$

with

$$\mathbf{K}_{\mathbf{u}\mathbf{u}} = \int_{V_e} \mathbf{B}_{\mathbf{u}}^T \mathbf{C} \mathbf{B}_{\mathbf{u}} + l^2 \mathbf{B}_{\nabla \mathbf{u}}^T \mathbf{G} \mathbf{B}_{\nabla \mathbf{u}} dV_e, \quad (52)$$

$$\mathbf{K}_{\mathbf{u}\boldsymbol{\phi}} = \mathbf{K}_{\boldsymbol{\phi}\mathbf{u}}^T = \int_{V_e} \mathbf{B}_{\mathbf{u}}^T \mathbf{e} \mathbf{B}_{\boldsymbol{\phi}} + \mathbf{B}_{\mathbf{u}}^T \mathbf{b} \mathbf{B}_{\nabla \boldsymbol{\phi}} + \mathbf{B}_{\nabla \mathbf{u}}^T \mathbf{F}^T \mathbf{B}_{\boldsymbol{\phi}} dV_e, \quad (53)$$

$$\mathbf{K}_{\boldsymbol{\phi}\boldsymbol{\phi}} = \int_{V_e} -\mathbf{B}_{\boldsymbol{\phi}}^T \mathbf{a} \mathbf{B}_{\boldsymbol{\phi}} - q^2 \mathbf{B}_{\nabla \boldsymbol{\phi}}^T \mathbf{H} \mathbf{B}_{\nabla \boldsymbol{\phi}} dV_e, \quad (54)$$

$$\mathbf{F}_{\mathbf{u}} = \sum_{a=1}^n \int_{\Gamma_t} N^a \mathbf{t} d\Gamma + \int_{\Gamma_R} n_j b_j^a \mathbf{R} b_i d\Gamma, \quad (55)$$

$$\mathbf{F}_{\boldsymbol{\phi}} = \sum_{a=1}^n \int_{\Gamma_S} N^a \mathbf{S} d\Gamma + \int_{\Gamma_Z} n_j b_j^a \mathbf{Z} d\Gamma. \quad (56)$$

Algorithm 1 presents schematically how the collocation method is implemented in UEL.

---

**Algorithm 1** Collocation method.

---

- 1: compute all  $\mathbf{J}^{-1}$  ▷ The inverse Jacobian matrix for all integration points (ip)
  - 2:
  - 3: compute  $\mathbf{B}_{\mathbf{u},N}$  according to Equation (27) ▷  $\mathbf{B}_{\mathbf{u},N}$  and  $\mathbf{B}_{\boldsymbol{\phi},N}$  contain the B-Matrices derived
  - 4: compute  $\mathbf{B}_{\boldsymbol{\phi},N}$  according to Equation (28) ▷ from nodal values  $N$  for all collocation points
  - 5:
  - 6: define  $\mathbf{A}^{-1}$  ▷ containing precalculated values of  $\mathbf{A}$  according to Equation (37)
  - 7:
  - 8: **for**  $1, \dots, n_{ip}$  **do** ▷ Loop over all ip
  - 9:
  - 10: compute  $\mathbf{P}$  according to Equation (32) ▷ The P-vector for current ip
  - 11:  $\mathbf{P} = (1, r_{ip}, s_{ip}, r_{ip} s_{ip})$
  - 12:
  - 13: compute  $\mathbf{P}_{,1}$  and  $\mathbf{P}_{,3}$  Equation (44) ▷ The directional derivatives
  - 14: ▷ of the P-vector for current ip
  - 15:  $\mathbf{P}_{,1} = (0, j_{11}^{inv}, j_{13}^{inv}, j_{11}^{inv} s_{ip} + j_{13}^{inv} r_{ip})$
  - 16:  $\mathbf{P}_{,3} = (0, j_{31}^{inv}, j_{33}^{inv}, j_{31}^{inv} s_{ip} + j_{33}^{inv} r_{ip})$  ▷ Use inverse Jacobian of current ip
  - 17:
  - 18: compute  $\mathbf{B}_{\mathbf{u}}$  according to Equation (41) ▷ The collocated  $\mathbf{B}_{\mathbf{u}}$ -matrix
  - 19:
  - 20: compute  $\mathbf{B}_{\nabla \mathbf{u}}$  according to Equation (42) ▷ The directional derivative of  $\mathbf{B}_{\mathbf{u}}$ -matrix
  - 21:
  - 22: compute  $\mathbf{B}_{\boldsymbol{\phi}}$  according to Equation (41) ▷ The collocated  $\mathbf{B}_{\boldsymbol{\phi}}$ -matrix
  - 23:
  - 24: compute  $\mathbf{B}_{\nabla \boldsymbol{\phi}}$  according to Equation (43) ▷ The directional derivative of  $\mathbf{B}_{\boldsymbol{\phi}}$ -matrix
  - 25:
  - 26: ...
  - 27: **end for**
-

### 3.2. CMFEM for Quadratic Element

In this subsection, CMFEM is derived for a quadratic element. In this quadratic element, quadratic shape functions [31] are used for interpolating the mechanical displacement and electric potential. This creates the possibility to assume the independent mechanical strains  $\varepsilon_{ij}$ , as well as the independent electric field  $E_i$  to be quadratic. So in this study, they are collocated over nine collocation points which are the  $3 \times 3$  Gaussian points 10,11,12,13,14,15,16,17,18 in Figure 3 [24]. For such an element,  $\mathbf{P}$ -vector could be defined as

$$\mathbf{P}(\mathbf{r}) = [ 1 \quad r \quad s \quad rs \quad r^2 \quad s^2 \quad r^2s \quad rs^2 \quad r^2s^2 ]. \quad (57)$$

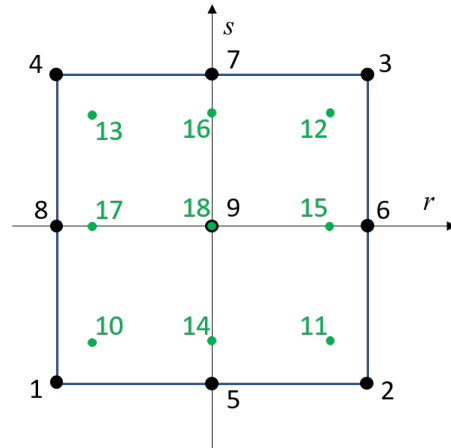


**Figure 3.** The nine-noded quadrilateral element in the local curvilinear coordinate system with  $3 \times 3$  Gaussian quadrature points.

The corresponding coefficient vectors take the following form where the left top index indicates that these are not the same coefficients as in Equations (33a) and (33e) :

$$\boldsymbol{\alpha}_{11} = [ {}^{13}\alpha \quad {}^{14}\alpha \quad \dots \quad {}^{21}\alpha ], \quad (58a)$$

$$\boldsymbol{\alpha}_{33} = [ {}^{22}\alpha \quad {}^{23}\alpha \quad \dots \quad {}^{30}\alpha ], \quad (58b)$$

$$\boldsymbol{\alpha}_{13} = [ {}^{31}\alpha \quad {}^{32}\alpha \quad \dots \quad {}^{39}\alpha ], \quad (58c)$$

$$\boldsymbol{\beta}_1 = [ {}^9\beta \quad {}^{10}\beta \quad \dots \quad {}^{17}\beta ], \quad (58d)$$

$$\boldsymbol{\beta}_3 = [ {}^{18}\beta \quad {}^{19}\beta \quad \dots \quad {}^{26}\beta ]. \quad (58e)$$

The  $\mathbf{A}$ -matrix changes to  $\mathbf{A} = \mathbf{A}_{quad}$  with  $\mathbf{A}_{quad}$  as

$$\mathbf{A}_{quad}^T = [ \mathbf{P}^T(\mathbf{r}_{10}) \quad \mathbf{P}^T(\mathbf{r}_{11}) \quad \dots \quad \mathbf{P}^T(\mathbf{r}_{17}) \quad \mathbf{P}^T(\mathbf{r}_{18}) ]. \quad (59)$$

The  $\mathbf{B}^a$ -matrices given in Equations (35) and (36) are required to be

$$\mathbf{B}_{\varepsilon_{11}}^{a,T}(\mathbf{r}_c) = \begin{bmatrix} b_1^a(\mathbf{r}_{10}) & b_1^a(\mathbf{r}_{11}) & \dots & b_1^a(\mathbf{r}_{17}) & b_1^a(\mathbf{r}_{18}) \\ 0 & 0 & \dots & 0 & 0 \end{bmatrix}, \quad (60a)$$

$$\mathbf{B}_{\varepsilon_{33}}^{a,T}(\mathbf{r}_c) = \begin{bmatrix} 0 & 0 & \dots & 0 & 0 \\ b_3^a(\mathbf{r}_{10}) & b_3^a(\mathbf{r}_{11}) & \dots & b_3^a(\mathbf{r}_{17}) & b_3^a(\mathbf{r}_{18}) \end{bmatrix}, \quad (60b)$$

$$\mathbf{B}_{\varepsilon_{13}}^{a,T}(\mathbf{r}_c) = \begin{bmatrix} b_3^a(\mathbf{r}_{10}) & b_3^a(\mathbf{r}_{11}) & \dots & b_3^a(\mathbf{r}_{17}) & b_3^a(\mathbf{r}_{18}) \\ b_1^a(\mathbf{r}_{10}) & b_1^a(\mathbf{r}_{11}) & \dots & b_1^a(\mathbf{r}_{17}) & b_1^a(\mathbf{r}_{18}) \end{bmatrix}, \quad (60c)$$

$$\mathbf{B}_{E_i}^{a,T}(\mathbf{r}_c) = [ b_i^a(\mathbf{r}_{10}) \quad b_i^a(\mathbf{r}_{11}) \quad \dots \quad b_i^a(\mathbf{r}_{17}) \quad b_i^a(\mathbf{r}_{18}) ]. \quad (60d)$$

The advantage of this quadratic element is that it can capture all mechanical strain gradient components in contrast to the linear element, which is only capable of calculating strain gradient components  $\eta_{133}$ ,  $\eta_{311}$ ,  $\eta_{131}$  and  $\eta_{313}$ . In the linear element, the components  $\eta_{111}$  and  $\eta_{333}$  cannot be captured. This means that the generated electric potential

due to flexoelectricity and the element stiffness is essentially more accurate with this quadratic element.

#### 4. Numerical Examples

This section investigates the performance of the linear and the proposed quadratic element. To begin with, the developed linear element is verified in the literature. A first numerical example serves the cantilever beam problem. Thereafter, the correctness of the quadratic element is verified by comparing it with the linear element results, setting particular strain gradient components to zero in the quadratic element. In a convergence study, the performance of both element types is evaluated, and the differences in the results are investigated and analyzed. Thereafter, a parameter study in which the influence of flexoelectric coefficients  $f_1$  and  $f_2$  on the deflection and the generated electric field measures both linear and quadratic elements. Finally, the performance of the newly developed quadratic element is illustrated on the truncated pyramid under the compression problem and verified with the literature.

##### 4.1. Cantilever Beam Problem

###### 4.1.1. Verification of Linear Element

In this subsection, the results obtained from the developed UEL, based on Section 3.1, are compared with the numerical results of the linear collocation mixed FEM element given in [25]. For this purpose, a nanoscaled cantilever beam problem with a transverse force on its end as in [25] is used as an example. The problem is assumed to be 2D plane strain.

As depicted in Figure 4, the beam has a length of  $L = 500$  nm, a width of  $B = 10$  nm a height of  $H = 20$  nm. The whole left side of the beam is horizontally fixed and one node is fixed in the vertical direction. At the free end of the beam over the right side, a force  $F$  is applied. Furthermore, the free end of the beam is electrically grounded. The boundary conditions are summarized in Table 1.

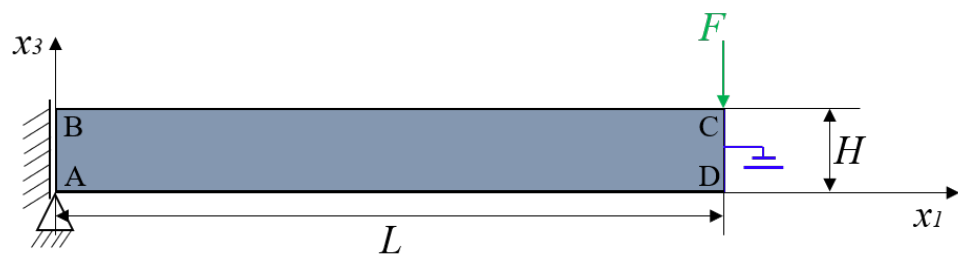


**Figure 4.** Cantilever beam model with transverse load  $F$  on its end.

**Table 1.** Boundary conditions and loads for the cantilever beam [25].

Side/Corner	Mechanical BC	Electrical BC	Prescribed Force
AB	$u_1 = 0$	-	-
A	$u_3 = 0$	-	-
CD	-	$\phi = 0$	$F = 1$ nN in $x_3$

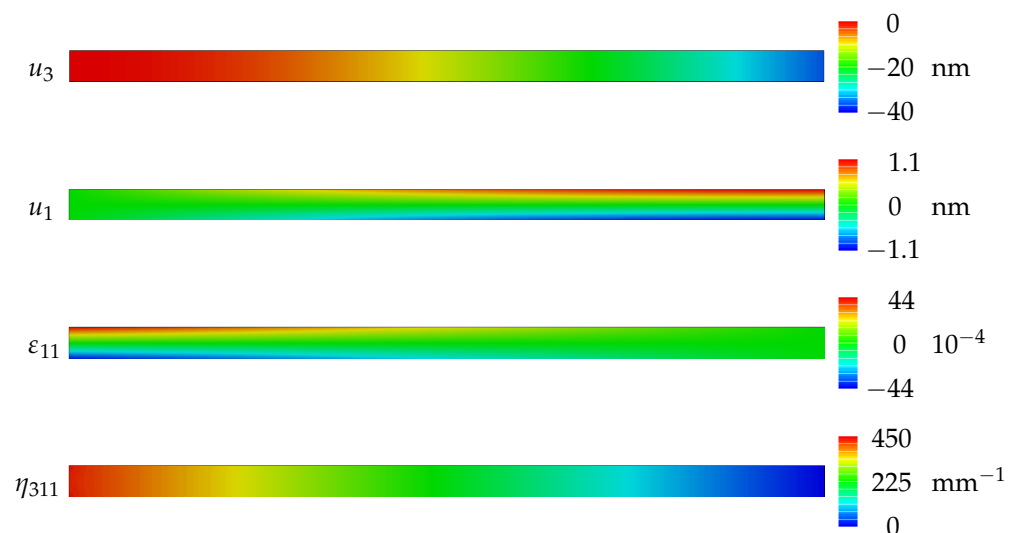
Piezoelectric material PZT-5H is used. As in [25], the material is chosen to be isotropic with parameters presented in Table 2.

**Table 2.** Material properties for the cantilever beam [25].

$E$ [GPa]	$\nu$ [-]	$l$ [nm]	$a_1, a_3$ [ $\frac{C^2}{Nm^2}$ ]	$f_1$ [ $\frac{\mu C}{m}$ ]	$f_2$ [ $\frac{\mu C}{m}$ ]
126	0	2	$13.0 \times 10^{-9}$	0.1	0

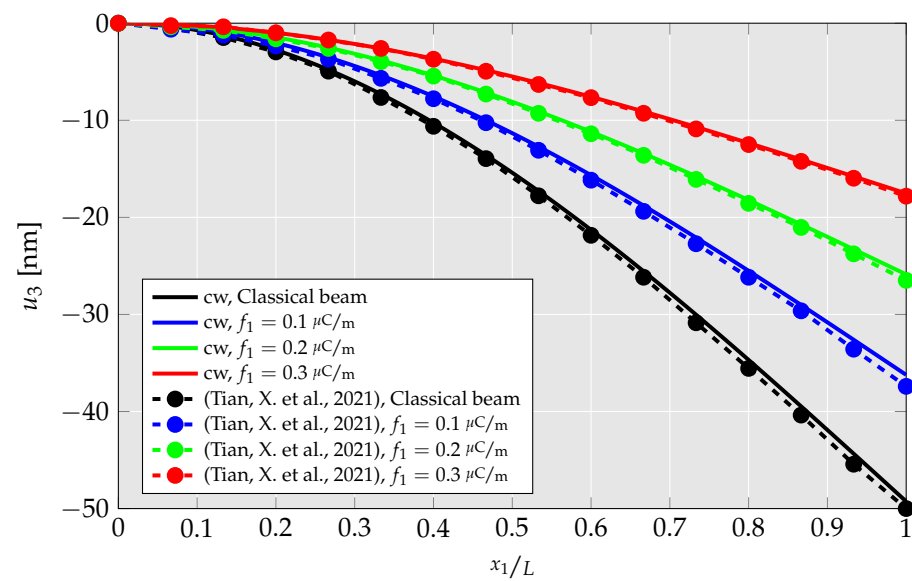
A Poisson's ratio of  $\nu = 0$  and not the stated value of  $\nu = 0.2$  is used for the cantilever beam simulation in [25]. This can be shown by analytical calculation of the deflection for the case of the linear elastic beam and comparing the result with the analytical solution given in the deflection plot. So  $\nu$  is set accordingly in the current work and only direct flexoelectricity is considered. In [25], 1600 elements for the cantilever beam are used. The same number of elements is used in the current simulations to compare both results better.

Figure 5 shows the distribution of the deflection components  $u_3$  and  $u_1$ , mechanical strain  $\varepsilon_{11}$ , and mechanical strain gradient  $\eta_{311}$  inside the cantilever beam. One can see that not only  $u_3$  but also  $u_1$  is built up and so there exists mechanical strain  $\varepsilon_{11}$ . The gradient of mechanical strain  $\varepsilon_{11}$  along  $x_3$  is much higher than any other mechanical strain gradient component, leading to the generation of the electric field.



**Figure 5.** Deflections  $u_3$  and  $u_1$ , mechanical strain  $\varepsilon_{11}$ , and mechanical strain gradient  $\eta_{311}$  distribution along the cantilever beam.

Deflection  $u_3$  of the cantilever beam along its length is presented in Figure 6 for different flexoelectric coefficients ( $f_1 = 0, f_1 = 0.1 \mu C/m, f_1 = 0.2 \mu C/m$  and  $f_1 = 0.3 \mu C/m$ ). It can be seen that by accounting for the mechanical strain gradient effect and increasing the flexoelectric coefficient  $f_1$ , the beam becomes stiffer and the deflection decreases.



**Figure 6.** Comparison of deflection of the cantilever beam between the results in the literature and of the current work using linear element for different flexoelectric coefficients  $f_1$ . “cw” denotes the current work.

The electrical response is shown in Figure 7. Electric potential is mainly built up on the fixed side of the beam where mechanical strain gradient  $\eta_{311}$  attains the highest value. In Figure 8, the electric field along the length of the cantilever beam is illustrated. One can see that the electric field has its maximum value at the fixed end and reduces linearly to the free end. From Figures 6 and 8 it is apparent that the results obtained with the developed code for the linear elements are in good agreement with the results presented in the literature.

However, with the linear element, only some components of the mechanical strain gradient tensor can be calculated correctly. This means some components are nearly zero, even if they should have a nonzero value. The reason for this lies in the coefficients of the independently assumed mechanical strains. In the case of linear elements, the mechanical strain gradient components  $\eta_{ij}$  are always zero because by taking the directional derivative of  $\varepsilon_{ij}$  along  $x_i$  only components of the  $\mathbf{P}$ -vector remain, the coefficients of which are zero. The idea is to get more accurate results by extending CMFEM by using quadratic shape functions for mechanical displacement and electric potential so that the element can capture all mechanical strain gradient components.

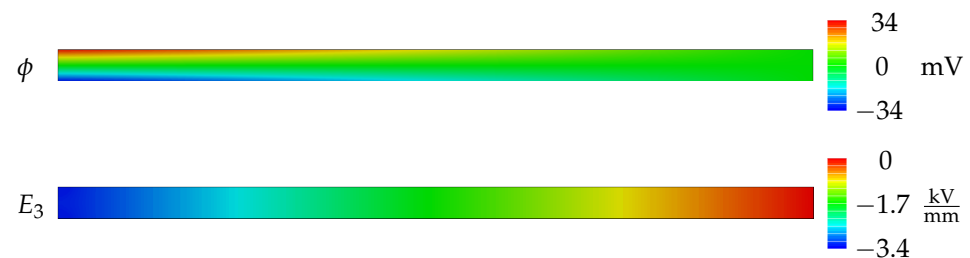


**Figure 7.** Electric potential  $\phi$  (top) and electric field  $E_3$  (bottom) distribution in the cantilever beam.

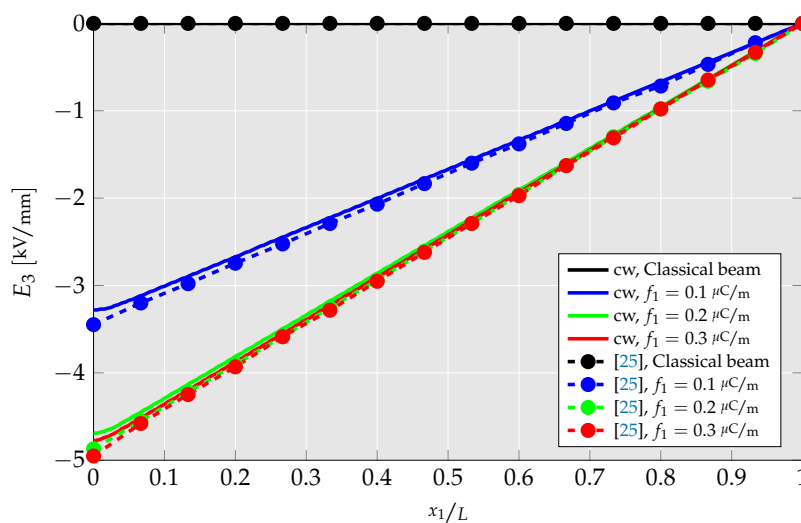


**Figure 8.** Comparison of electric field of the cantilever beam between the results given in the literature and of the current work by using linear element for different flexoelectric coefficients  $f_1$ . cw denotes the current work.

#### 4.1.2. Comparison of Linear and Quadratic Elements

At this point, it is essential to compare the performance of linear and quadratic elements with relevant boundary value problems (BVP). The numerical results are analyzed and compared with those in the corresponding literature. In this subsection, only those strain gradient components are considered which are nonzero in the linear elements. Other mechanical strain gradient components are hardcoded as zeros in the UEL for the quadratic element. From this, we can make the closest comparison with the known linear element behavior (cf. Section 4.1.1). The full calculation without such restrictions are presented in Section 4.1.4.

In Figures 9 and 10, the displacement  $u_3$  and electric field  $E_3$  are presented for different flexoelectric coefficients. Both quantities are measured at  $x_3 = H/2$  along the length of the beam. It can be seen that with an increasing value of  $f_1$ , the mechanical displacement reduces and the electric field increases. Although there is a negligibly small difference in the results of the linear element and the analytical solution, the results of the quadratic element appear to be in very good agreement with the linear element.

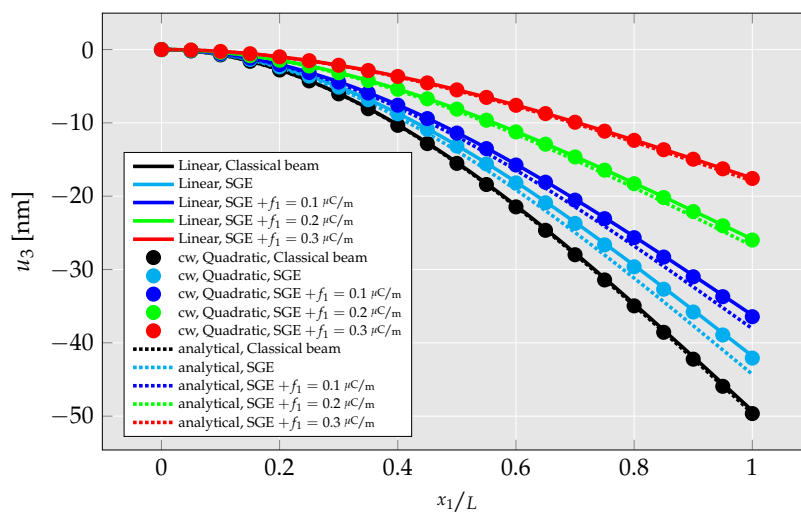


**Figure 9.** Deflection  $u_3$  of the cantilever beam for linear and quadratic element with neglected strain gradient components, along with analytical solution. cw denotes the current work.

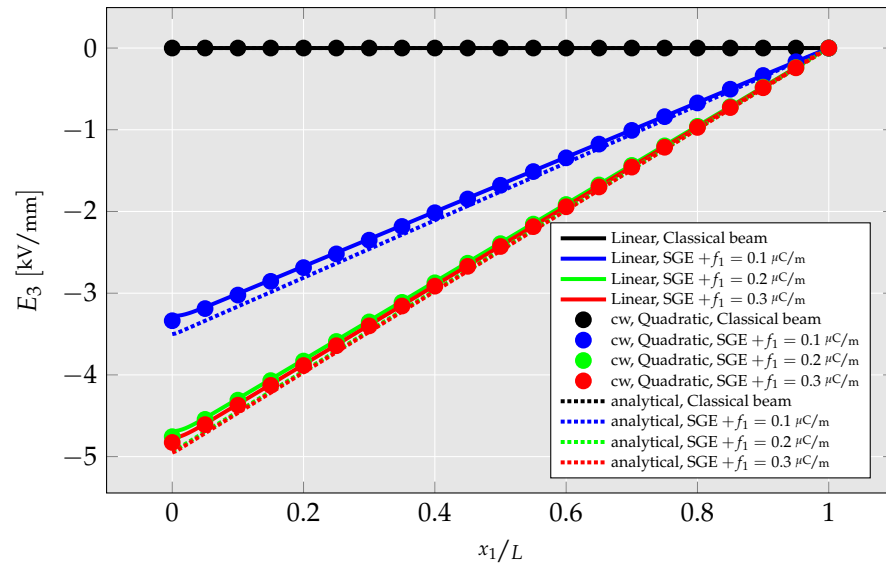


**Figure 10.** Electric field  $E_3$  generated in the cantilever beam for linear and quadratic element with neglected strain gradient components vs. analytical solution. cw denotes the current work.

#### 4.1.3. Convergence Study

A convergence study is made to compare the linear and quadratic elements. The relative error between numerical results for developed linear and quadratic elements and the analytical solution is analyzed for different mesh sizes. For this convergence study the same parameters for the cantilever beam problem is used as described in Tables 1 and 2 with  $f_1 = 0.1 \mu\text{C}/\text{m}$  and  $f_2 = 0$ .

The relative error  $e(\mathbf{X})$  of the numerical simulations is calculated by using the  $l_2$ -norm

$$e(\mathbf{X}) = \frac{\|\mathbf{X}^s - \mathbf{X}\|_{l_2}}{\|\mathbf{X}\|_{l_2}} \tag{61}$$

where

$$\|\mathbf{X}\|_{l_2} = \sqrt{\int_{\Omega} \mathbf{X}^T \mathbf{X} d\Omega}. \tag{62}$$

$\mathbf{X}^s$  represents the numerical results and  $\mathbf{X}$  is the analytical solution. As a reference solution, the analytical results for the deformation of a Bernoulli–Euler beam are chosen where only the result for direct flexoelectricity is available. The deflection of the flexoelectric cantilever beam is given by [11]

$$u_3(x_1) = C_1 + C_2x_1 + C_3(x_1)^2 + C_4(x_1)^3 + C_5 \exp\left(\frac{\lambda x_1}{L}\right) + C_6 \exp\left(-\frac{\lambda x_1}{L}\right), \tag{63a}$$

$$\lambda^2 = \frac{c_{11}I + \left(c_{11}l^2 + \frac{f_1^2}{a_3}\right)BH}{c_{11}l^2I} L^2. \tag{63b}$$

The exponent of  $L$  is corrected in [25] and the correct sign is taken from [11]:  $C_4 = -\frac{FL^2}{6\lambda^2 g_{11}I}$ .

The analytical solution for the generated electric field is given by [11]

$$E_3 = -\frac{f_1}{a_3} \eta_{311}. \tag{64}$$

However, this analytical solution depends only on  $x_1$ , whereas the numerical results are a function of both  $x_1$  and  $x_3$ . Consequently, the quadratic element is considered more

accurate than the analytical solution [25]. For the convergence analysis, eight different meshes are analyzed, including 25, 100, 225, 400, 625, 900, 1225, and 1600 elements, respectively. Figure 11 illustrates the finest and roughest mesh used.

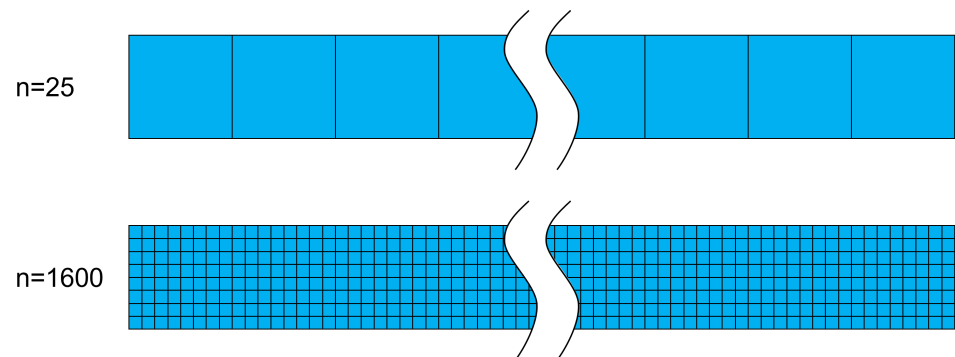


**Figure 11.** Coarse (top) and fine (bottom) mesh used for the convergence analysis of the cantilever beam problem with total element number  $n$ . Not all elements are shown for better visualization.

Figure 12 shows the relative error for the displacement  $u_3$  and electric field  $E_3$  for both element types with different average element length  $h$ , which is calculated from the total number of elements in the current mesh  $n$  as  $h = \sqrt{HL/n}$ . It can be seen that the results for the linear elements are strongly mesh-dependent, and hence the relative error is higher for a mesh model with fewer elements. The relative error of the quadratic element is lower than the linear element, regardless of the coarseness of the meshed model. As presented, the accuracy of the results of the quadratic element is way higher than that of the linear element. This is expressed by the fact that the low accuracy of the linear elements when using a coarse mesh increases by increasing the fineness of the mesh, but even for a very fine mesh, it does not reach the performance of the quadratic elements for a very coarse mesh. The accuracy of quadratic elements, on the other hand, is the same for the coarsest and finest mesh.

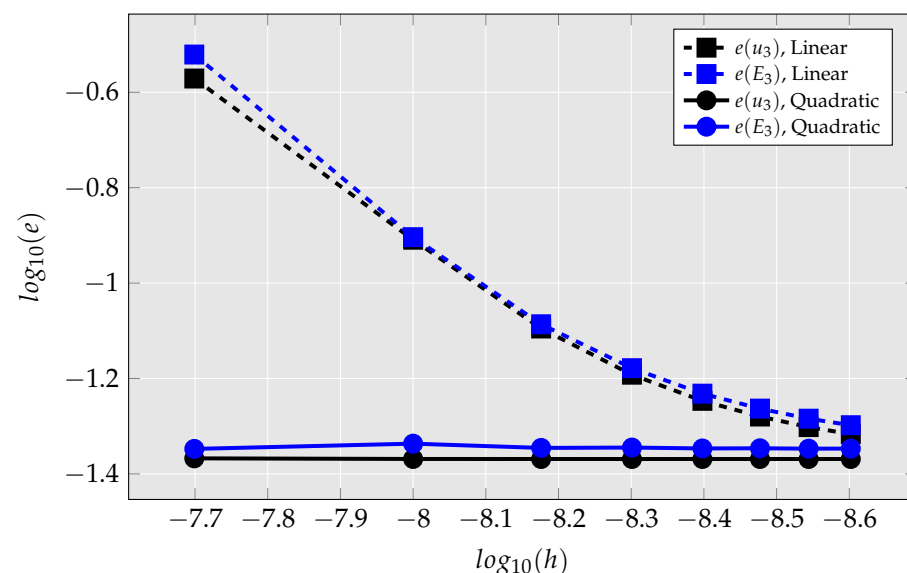


**Figure 12.** Relative errors and convergence rates of displacement  $u_3$  and electric field  $E_3$  for the developed linear and quadratic element with neglected strain gradient components.

#### 4.1.4. Investigation of Differences between Linear and Quadratic Elements

For the analysis performed in this and further sections, the mechanical strain gradient components  $\eta_{ij}$  are no longer set to zero as in Section 4.1.2. Furthermore, apart from a

Poisson's ratio of  $\nu = 0.3$ , the boundary conditions of Table 1 and material properties of Table 2 are used.

The deflection and the electric field generated in the cantilever beam are presented for SGE with flexoelectricity  $f_1 = 0.1 \mu\text{C}/\text{m}$  in Figures 13 and 14, respectively. It can be observed that the compliance of the beam for the quadratic element is increased compared to the linear element. Due to oversimplification of the derivations for the linear elements, the electromechanical coupling is overestimated by the linear element and therefore the electric field for the linear element is higher compared to that of the quadratic element.

Displacement of  $u_3 = 40 \text{ nm}$  is prescribed for the cantilever beam to find the cause for the differences in the current investigation results. The resulting mechanical strains are presented in Figure 15 and is measured at  $x_1 = 0.1L$  along the height of the beam. It can be seen that mechanical strain  $\varepsilon_{11}$  rises,  $\varepsilon_{33}$  reduces and  $\varepsilon_{13}$  is nearly the same. Strain  $\varepsilon_{33}$  insignificantly differs at the edges for the linear elements compared to the quadratic element. The reason for this is explained in Section 4.1.6 (cf. Figure 27). The magnitude of all mechanical strain components is the same for the linear and quadratic elements. For the stress components, both types of elements gave similar results (Figure 16). The reason for the small difference in stress components  $\sigma_{11}$ ,  $\sigma_{22}$  and  $\sigma_{33}$  at the edges is the same as mentioned above for strain component  $\varepsilon_{33}$ .

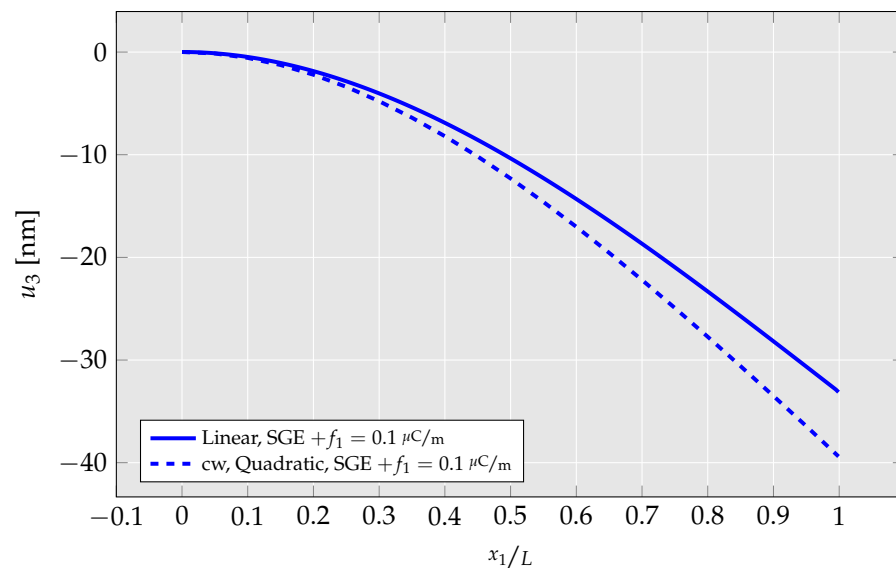


**Figure 13.** Comparison of deflection calculated by using linear and quadratic element along the length of the beam.

However, differences in calculated mechanical strain gradients using linear and quadratic elements are illustrated in Figure 17. For comparison reasons, in these cantilever beam simulations the material parameters of [25] are used where only the influence of  $f_1$  is considered which means that  $f_2$  is set to be zero. Consequently, according to Equation (68), the mechanical shear strains have in this example no direct influence on the magnitude of the generated electric field  $E_3$ . Therefore, only the gradients of  $\varepsilon_{11}$ ,  $\varepsilon_{33}$  are considered for both element types in the following analysis.

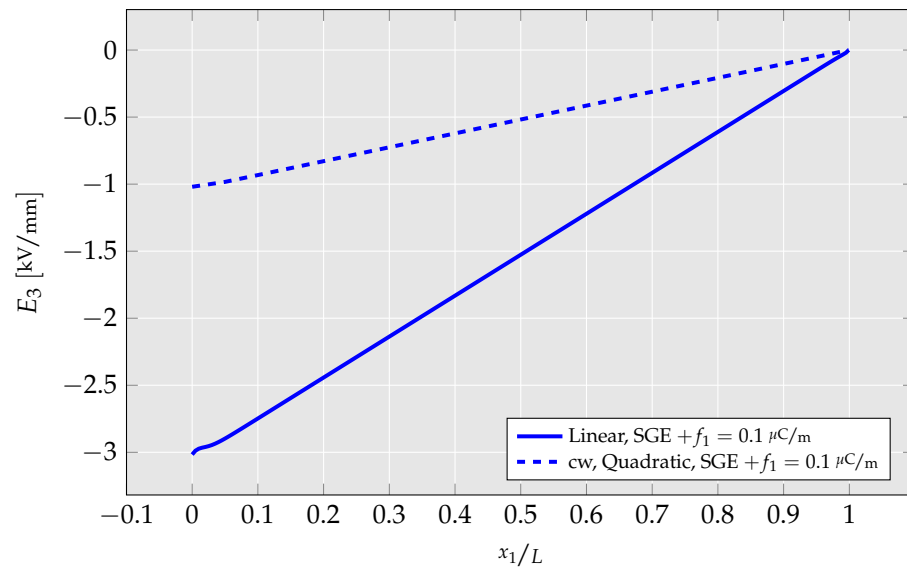


**Figure 14.** Comparison of electric field calculated by using linear and quadratic element along the length of the beam.

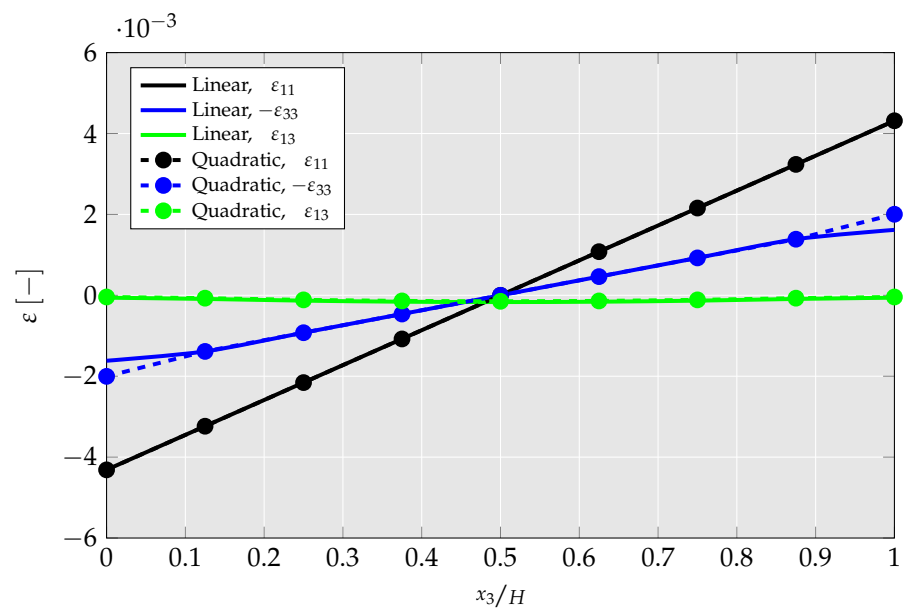


**Figure 15.** Comparison of the mechanical strain components calculated by using linear and quadratic element through the height of the beam for prescribed mechanical displacement.

In this numerical example, among all the components of mechanical strain gradients, only the two components  $\eta_{311}$  and  $\eta_{333}$  are of relevant magnitude. Strain gradient  $\eta_{311}$  is a consequence of the distribution of mechanical strain  $\epsilon_{11}$  that results from the bending of the beam caused by the prescribed displacement  $u_3$ . When  $u_3$  is prescribed, the bending of the beam is the same for the linear and quadratic element, so  $\eta_{311}$  is identical in both cases. Because of the usage of the nonzero Poisson’s ratio, mechanical strain  $\epsilon_{33}$  is built up that varies along  $x_3$  inside the cantilever beam, as shown in Figure 18. This results in a strong mechanical strain gradient  $\eta_{333}$  at the beam’s left side, which reduces toward the free end. In contrast to the quadratic element, the linear element is unable to capture this mechanical strain gradient component. A comparison of the mechanical strain gradient  $\eta_{333}$  distribution is presented in Figure 19.

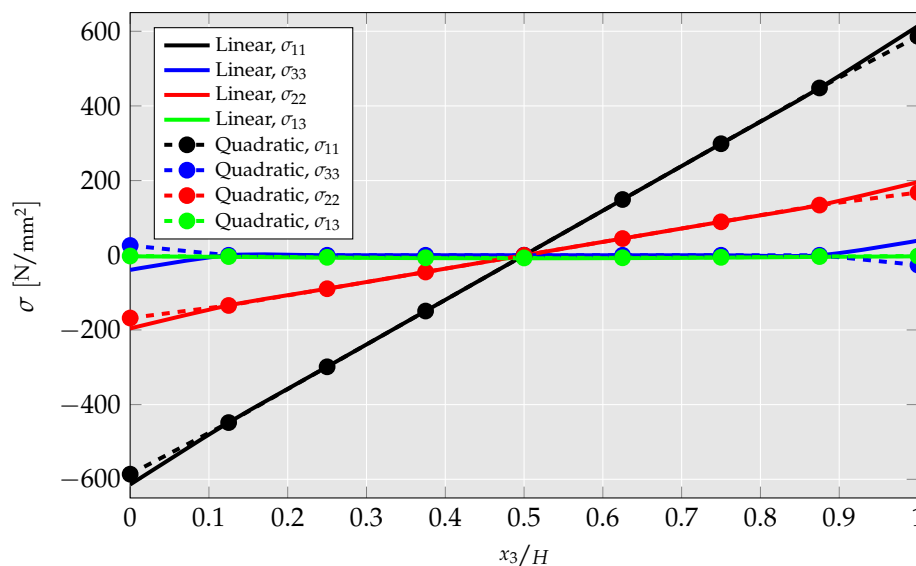


**Figure 16.** Comparison of mechanical stress components calculated by using linear and quadratic element along the height of the beam for prescribed mechanical displacement.

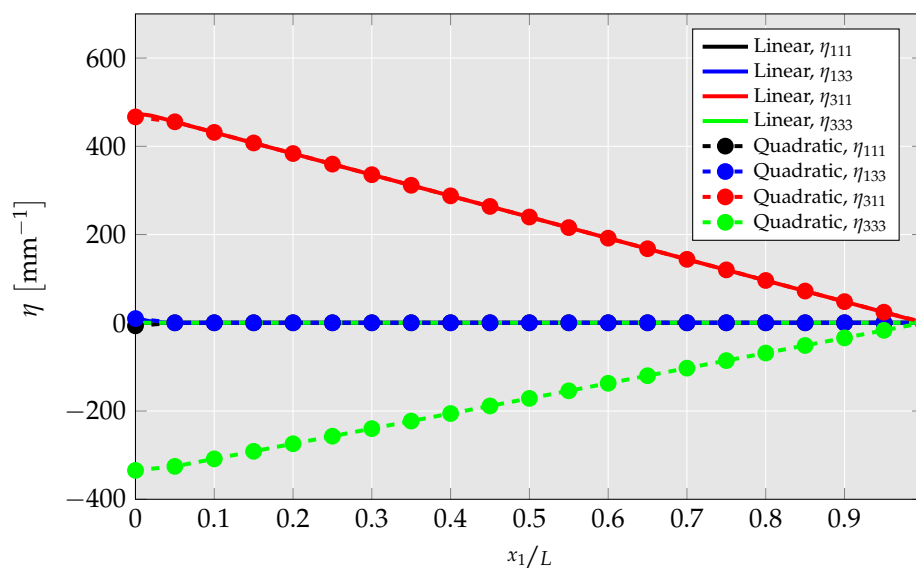


**Figure 17.** Comparison of mechanical strain gradient components calculated by using linear and quadratic element along the length of the beam for prescribed mechanical displacement.

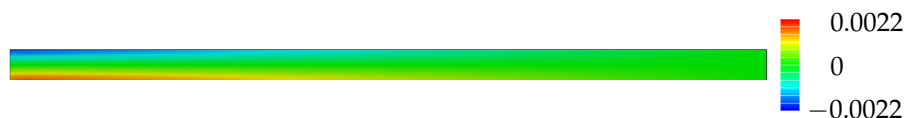


**Figure 18.** Mechanical strain  $\epsilon_{33}$  distribution along the cantilever beam.



**Figure 19.** Comparison of mechanical strain gradient  $\eta_{333}$  distribution for the linear (top) and quadratic (bottom) element along the cantilever beam.

The inability of the linear element to capture this mechanical strain gradient yields comparatively different higher-order stress in contrast to quadratic elements visible in

Figure 20. The higher-order stress  $\tau$  is measured along the length at the midheight of the beam. It can be observed that both higher-order stress components  $\tau_{311}$  and  $\tau_{333}$  reduce for the quadratic element, in particular  $\tau_{333}$  nearly vanishes. The components  $\tau_{111}$  and  $\tau_{133}$  remain zero. This reduces the beam's stiffness, which explains the beam's higher deflection for the quadratic element (Figure 13). Based on Equation (15c), the higher-order stress exclusively depends on the contributions from flexoelectrical coupling and pure SGE as

$$\tau = \tau^f + \tau^g, \quad (65)$$

where the flexoelectric contribution is denoted with "f" and that from SGE with "g". For  $\tau_{311}$  and  $\tau_{333}$ , flexoelectric contributions are

$$\tau_{311}^f = -f_1 E_3, \quad (66a)$$

$$\tau_{333}^f = -(f_1 + 2f_2) E_3 \quad (66b)$$

and the SGE contributions can be written as

$$\tau_{311}^g = l^2(c_{11}\eta_{311} + c_{13}\eta_{333}), \quad (67a)$$

$$\tau_{333}^g = l^2(c_{13}\eta_{311} + c_{33}\eta_{333}). \quad (67b)$$

Figure 21 compares the contributions between linear and quadratic elements to investigate the reason for the difference in higher-order stresses.

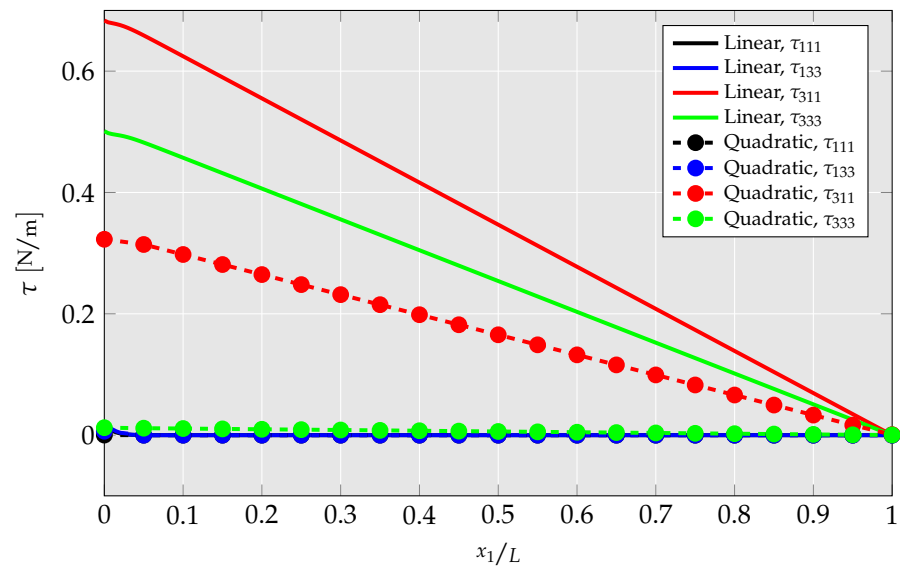


**Figure 20.** Comparison of higher-order stress components calculated by using linear and quadratic element along the length of the beam for prescribed mechanical displacement.

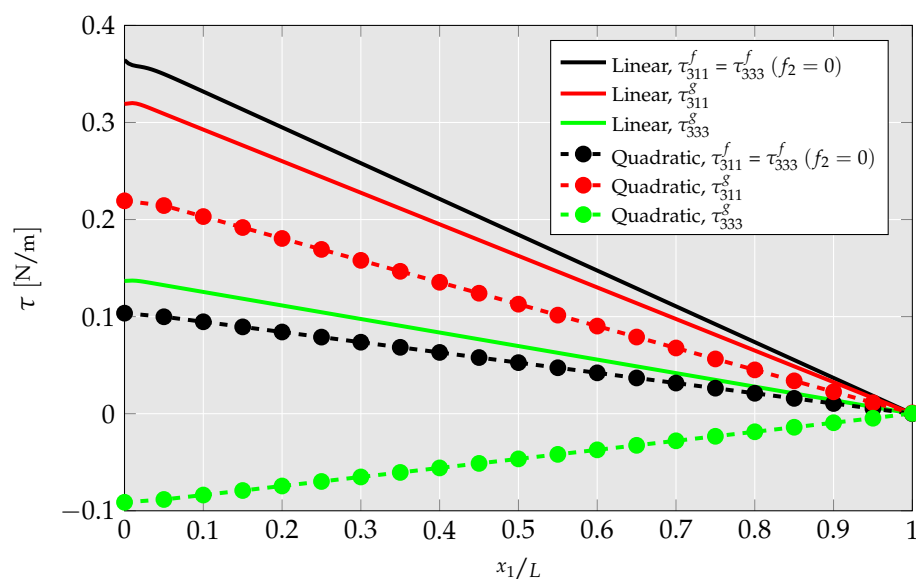


**Figure 21.** Flexoelectric and mechanical strain gradient contributions to the higher-order stress components  $\tau_{311}$  and  $\tau_{333}$  for linear and quadratic element along the length of the beam for prescribed mechanical displacement.

The flexoelectric contribution to higher-order stress is the same for  $\tau_{311}$  and  $\tau_{333}$  when  $f_2 = 0$ , cf. Equation (66).  $\tau_{311}^f$  and  $\tau_{333}^f$  reduce proportionally to the electric field  $E_3$  as seen in Figure 22. Furthermore, the SGE contribution to higher-order stress differs for linear and quadratic elements because of the nonzero component  $\eta_{333}$  in the quadratic elements (cf. Equation (67)). As a result, the contribution of SGE and flexoelectricity effectively cancel each other for higher-order stress  $\tau_{333}$  as illustrated in Figure 20.

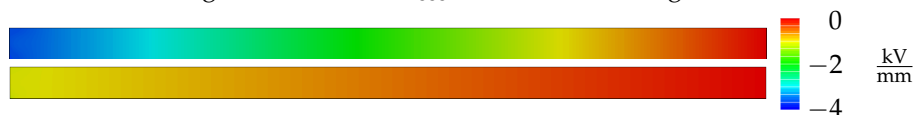


**Figure 22.** Comparison of electric field  $E_3$  distribution based on linear (top) and quadratic (bottom) element in the cantilever beam.

The resulting change in electric displacement that is measured along the height at  $x_1 = 0.1 L$  can be seen in Figure 23. For the quadratic element, electric displacement  $D_1$  reduces while  $D_3$  is zero for both element types along the height of the beam. The reason, for  $D_3$  to come out to be zero, is that at the top and bottom side of the cantilever beam no electric potential is prescribed. If  $D_3$  is zero and there is no piezoelectricity involved, Equation (15b) simplifies to the following formula for the electric field  $E_3$ :

$$E_3 = -\frac{f_1}{a_3}(\eta_{311} + \eta_{333}) - \frac{2f_2}{a_3}(\eta_{113} + \eta_{333}). \tag{68}$$

The resulting electric field for the quadratic element is drastically reduced compared to the linear element. The reason for this is that the mechanical strain gradient component  $\eta_{333}$  can be captured with quadratic elements and has a nonzero value. Additionally,  $\eta_{333}$  has a sign opposite to  $\eta_{311}$ , as can be seen in Figure 17. This explains the difference in intensity of the electric field in Figure 14. In this numerical example  $f_2$  is omitted as in [25].

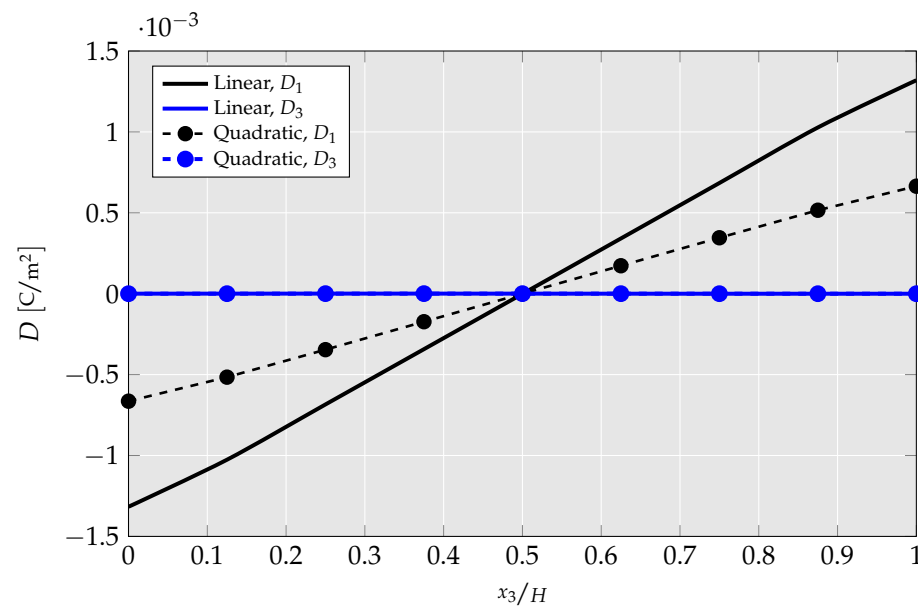


**Figure 23.** Comparison of electric displacement components calculated by using linear and quadratic element along the height of the beam for prescribed mechanical displacement.

#### 4.1.5. Parameter Study of Flexoelectric Coefficients

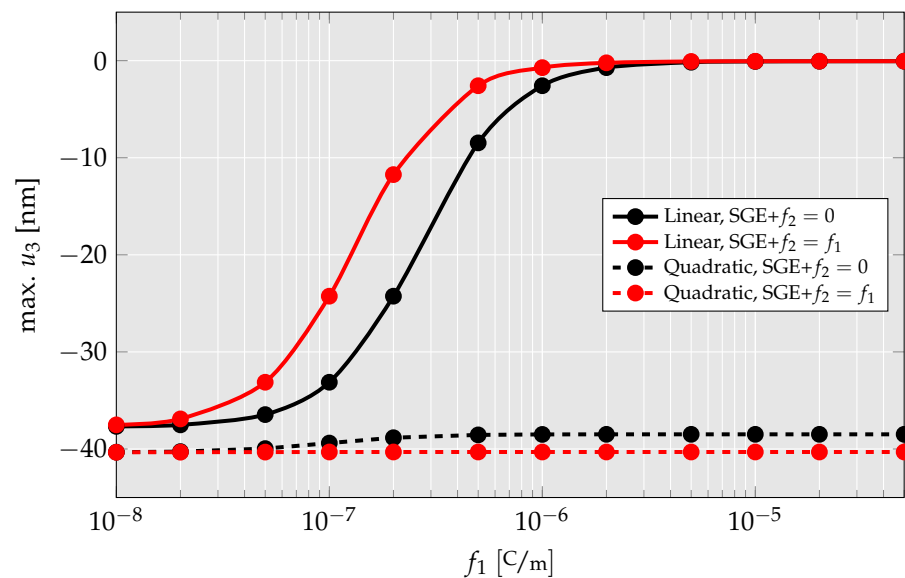
In this subsection, the influence of flexoelectric coefficients in case of the cantilever beam problem described in Section 4.1.1 is studied. The boundary conditions of Table 1 and material properties of Table 2 with Poisson's ratio  $\nu = 0.3$  are used. For both element types, two simulation series are performed in which the flexoelectric coefficient  $f_1$  varies between 0.01 and 50.0  $\mu\text{C}/\text{m}$ . For one case scenario,  $f_2 = 0$  as commonly supposed in the literature [25,32,33], whereas for the other,  $f_1$  and  $f_2$  are equal.

Figure 24 shows the maximum displacement  $u_3$  for different flexoelectric coefficients. The flexoelectric coefficient axis has a logarithmic scale to cover a wider span of flexoelectric coefficients. One can see that for the linear element the flexoelectric influence is negligible when  $f_1$  and  $f_2$  are smaller than 0.02  $\mu\text{C}/\text{m}$ . From  $f_1 = 0.05 \mu\text{C}/\text{m}$ , the influence of flexoelectricity on the beam's stiffness increases until at  $f_1 = 2 \mu\text{C}/\text{m}$  the beam becomes so stiff that the maximum deflection saturates nearing zero. When  $f_1$  and  $f_2$  are equal, this saturation value is reached for even smaller flexoelectric coefficients. On the other hand, the quadratic element's maximum deflection reaches a saturation value at 39 nm when  $f_2 = 0$ . When  $f_2 = f_1$ , the value of the flexoelectric coefficients has negligible influence on the beam's stiffness.

The electric field for different values of the flexoelectric coefficient  $f_1$ , measured at the fixed end, is presented in Figure 25. It can be seen that in the area of the small flexoelectric coefficients, the magnitude of the electric field increases alongside the stronger flexoelectric coupling. However, the electric field magnitude reaches a maximum value and with further increased flexoelectric coefficients, the generated electric field inside the beam gets closer to zero again.

Because from a physical standpoint the flexoelectric coefficients describe the ability of the center atom in a unit cell to break the symmetry and to generate an electric field as a result of the application of strain gradients, it is expected that for higher flexoelectric coefficients this center atom can move easier. From a numerical standpoint, strain gradient components  $\eta_{311}$  and  $\eta_{333}$  arise from the bending of the cantilever beam. However, if Poisson's ratio is zero [12,16,25],  $\eta_{333}$  is not generated. When SGE is involved,  $\eta_{311}$  and  $\eta_{333}$  build up higher-order stress  $\tau_{311}$  and  $\tau_{333}$ , as stated in Equation (67). Due to flexoelectricity, both strain gradient components contribute to the generation of an electric field  $E_3$  (cf. Equation (68)). However, because of the two-way coupling of flexoelectricity, this generated electric field  $E_3$  again influences  $\tau_{311}$  and  $\tau_{333}$ , which affects the strain gradient components

$\eta_{311}$  and  $\eta_{333}$ . As can be seen in Equation (66), the pure flexoelectric contribution to higher-order stress components  $\tau_{311}$  and  $\tau_{333}$  is identical when  $f_2 = 0$ . When considering that for high flexoelectric parameters the pure flexoelectric contribution to higher-order stresses becomes more dominant compared to the SGE contribution, this leads to the corresponding strain gradients in a way that the magnitude of both strain gradients  $\eta_{311}$  and  $\eta_{333}$  become closer in magnitude. As can be seen in Figure 17,  $\eta_{311}$  and  $\eta_{333}$  have the opposite sign, which leads to their sum nearing zero for higher flexoelectric coefficients.



**Figure 24.** Maximum deflection  $u_3$  of the cantilever beam calculated by using linear and quadratic element for various flexoelectric coefficients.

With  $C^1$ -continuity,  $\eta_{333}$  not only influences the strains inside each element separately, but also influences the other results of the cantilever beam. This would lead to an electric field which saturates at a specific value. When the strains are not continuous from element to element, the magnitude of  $\eta_{333}$  due to the presence of  $E_3$  is overestimated, as discussed in Section 4.1.6. This leads to the sum of  $\eta_{311}$  and  $\eta_{333}$  nearing zero at a faster rate than the flexoelectric coefficients increase. According to Equation (68), this leads to a reduction of electric field which explains why  $E_3$  is nearing zero for high flexoelectric coefficients. In case of  $C^1$ -continuity, this behavior would be more balanced out in a way that the electric field reaches a saturation value. Because by using the linear element,  $\eta_{333}$  is always zero, for high flexoelectric parameters, the sum of both strain gradient components only reaches zero when  $\eta_{311}$  becomes zero, too. Mechanical strain gradient  $\eta_{311}$  describes the change of  $\varepsilon_{11}$  along  $x_3$  resulting from the bending of the cantilever beam as visualized in Figure 5.

Figure 26 depicts the normalized deflection  $u_{\text{norm}} = \frac{u_3}{|u_{3,\text{max}}|}$  of the cantilever beam for both linear and quadratic elements for  $f_1 = 0.1 \mu\text{C}/\text{m}$  and  $f_1 = 50.0 \mu\text{C}/\text{m}$ .

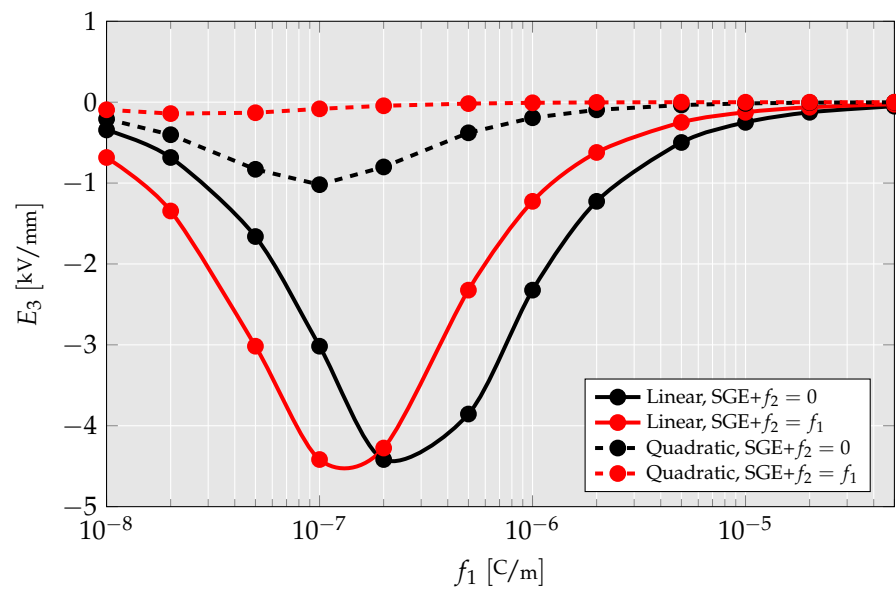


**Figure 25.** Maximum electric field  $E_3$  of the cantilever beam calculated by using quadratic element for various flexoelectric coefficients.

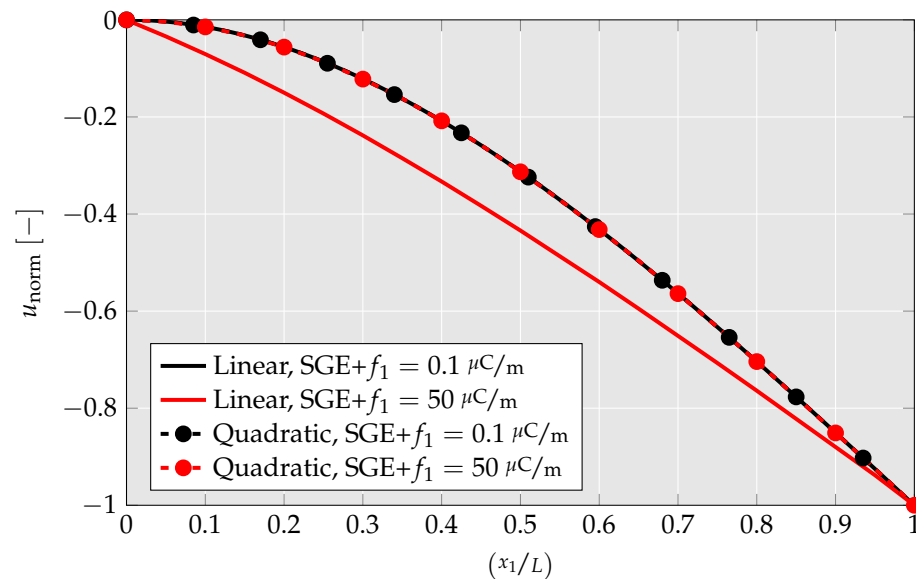


**Figure 26.** Comparison of cantilever beam bending for a small and high flexoelectric coefficient by using the linear and quadratic element.

One can see in Figure 26 that in the linear case in which there is nearly no deflection at all (cf. Figure 24), the stiffness of the beam becomes so high that there is nearly no bending of the beam. In contrast, there is no difference in the normalized bending profile between low- and high-flexoelectric coefficients for the quadratic element. This means that  $\eta_{311}$  is proportionally reduced compared to the quadratic element. To sum up this subsection, the linear element is not suitable for flexoelectric simulations because of its inability to capture all strain gradient components, though for correct flexoelectric simulations, it is necessary to calculate all strain gradient components correctly. By using quadratic shape function for the DOFs and assuming the independent mechanical strain and electric field of a quadratic shape, the quadratic element can compute all strain gradient components. Thereby, it can simulate a physically more realistic flexoelectric behavior. However, the quadratic element can be further improved by ensuring  $C^1$ -continuity as discussed in Section 4.1.6.

#### 4.1.6. Discussion about the Advantages of Quadratic Element

As mentioned in Section 4.1.4, the linear and quadratic elements' behavior partially differs. This is because the quadratic element can capture all mechanical strain gradient components, which is a priori not possible with the linear element. A higher resolution of  $\varepsilon_{33}$  is presented in Figure 27. The mechanical strain gradient  $\eta_{333}$  behavior for linear and quadratic cases is represented by the slope of  $\varepsilon_{33}$  for each element.

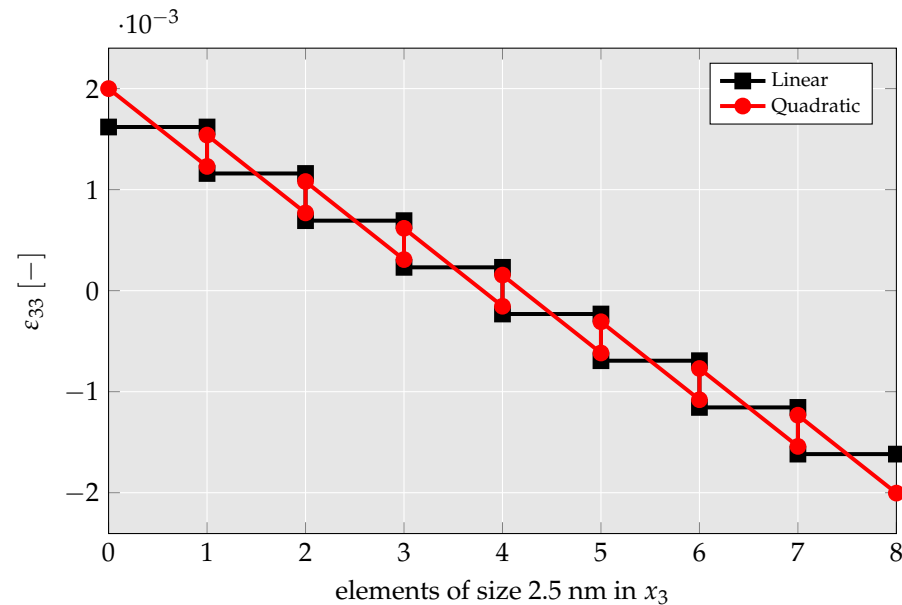


**Figure 27.** Discontinuous strain  $\varepsilon_{33}$  for linear and quadratic element across the height of the cantilever beam.

For the linear element, the mechanical strain in each element is constant; hence, the mechanical strain gradient is zero, whereas for the quadratic element, the mechanical strain inside each element is no longer a constant. The gradient in each element is slightly higher than the overall mechanical strain gradient along the height of the beam. Consequently, the linear element is not suitable for the description of some relevant strain gradient components. The quadratic element is able to describe all of the components and only overestimates slightly those mechanical strain gradient components that the linear element does not capture. However, calculating the correct mechanical strain gradients is important because in coupled systems like flexoelectricity, incorrectly calculated strain gradients lead to drastically different results of mechanical displacement, electric potential, and their derived quantities. The quadratic element is capable of simulating a realistic flexoelectric material behavior. Further improvement can be achieved by ensuring  $C^1$ -continuity.

#### 4.2. Truncated Pyramid Compression Problem

Another typical example of modeling flexoelectricity is a truncated pyramid [8,34]. Because of the different sizes of the top and bottom surfaces, applied stress on the top surface distributes toward the bottom surface, generating mechanical strain gradients.

Similar to the cantilever beam example, this is a plane strain problem for direct flexoelectricity ( $q = 0, b_1 = b_2 = b_3 = 0$ ). The truncated pyramid has a height  $h$ , a top surface of length  $h$  and a bottom surface of length  $3h$ . The angle between the bases and the oblique surfaces is  $\pi/4$ . The bottom surface is fixed in all directions. For compressing the pyramid, a constant linear force  $F$  is prescribed on the top surface, as illustrated in Figure 28. Furthermore, the pyramid is electrically grounded on the top surface. Due to the different sizes of the top and bottom surfaces, strain gradients build up which generate an inhomogeneous electric potential  $\phi$  distribution. Typically, opposite the grounded surface, a sensing electrode is attached. This electrode equals the electric potential on this surface

to a constant value which is not known a priori. The boundary conditions as in [16] are summarized in Table 3.

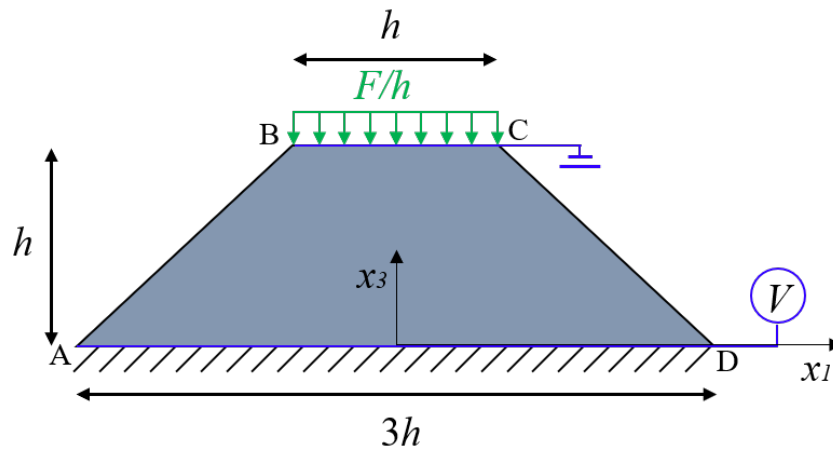


Figure 28. Truncated pyramid model with compressive load on top.

Table 3. Boundary conditions for the truncated pyramid.

Side	Mechanical BC	Electrical BC	Prescribed Force
AD	$u_1 = u_3 = 0$	$\phi = V = \text{const}$	-
BC	-	$\phi = 0$	$F = 4.5 \frac{\text{N}}{\text{mm}}$ in $x_3$

The material properties used are shown in Table 4. All simulation results are obtained for a mesh model containing 2500 elements.

Table 4. Material properties for the truncated pyramid [16].

$E$ [GPa]	$\nu$ [-]	$l$ [nm]	$a_1, a_3 [\frac{\text{C}^2}{\text{Nm}^2}]$	$f_1 [\frac{\mu\text{C}}{\text{m}}]$	$f_2 [\frac{\mu\text{C}}{\text{m}}]$
100	0.37	0	$11.0 \times 10^{-9}$	1.0	0

The results in Figures 29 and 30 are obtained for  $h = 7.5 \mu\text{m}$ . The contour plots of the mechanical strain  $\epsilon_{33}$  and electric potential  $\phi$  are shown in Figure 29 for the linear and quadratic element. It can be observed that the mechanical strain is identical for both elements. In contrast, the electric potential using linear element is reduced by approximately 230% compared to the quadratic element and the reference solution [35]. Not only are higher maximum values reached by using the linear element, but the nature of the electric field distribution is physically invalid (cf. Figure 29 bottom right), even leading to a negative electric potential at the bottom part of the pyramid.

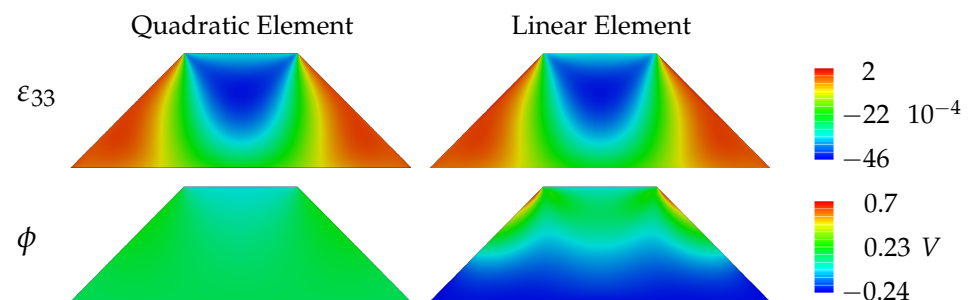
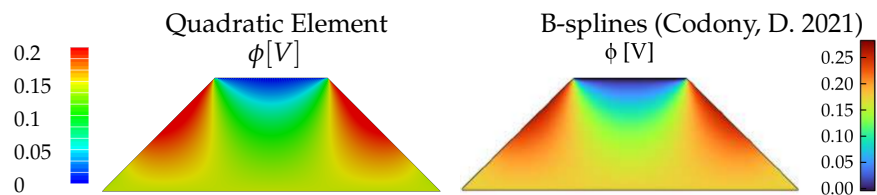


Figure 29. Contour plots for mechanical strain  $\epsilon_{33}$  and electric potential  $\phi$  in the truncated pyramid using linear and quadratic elements. The same color scale is used for both elements for better comparison.



**Figure 30.** Contour plots of the electric potential  $\phi$  in the truncated pyramid by [16,35] vs. the use of the developed quadratic element. The color scale for the contour of the quadratic element is adjusted for a higher contrast image.

Figure 30 shows the contour of the electric potential  $\phi$  for the same simulation using the quadratic element as in Figure 29 but with an adjusted scale for comparison with the results obtained using B-spline method [16,35]. One can see that the nature of the distribution of the electric field for the quadratic element is in good agreement with the results of the B-spline formulation. However, small differences in the electric potential distribution can be observed. For example at midheight, the electric potential gradient in  $x_1$ -direction from the center to the oblique sides is higher using quadratic elements. This phenomena is physically more realistic, as can be seen in the computational results of [36].

Furthermore, an effective electric field  $E_{\text{eff}} = V/h$  can be calculated, which is the voltage difference between the top and bottom bases. Figure 31 shows the effective electric field for different sizes of the truncated pyramid. For this simulation series, the line force  $F$  mentioned in Table 3 is used while  $h$  is different for each simulation. For different pyramid sizes the mechanical strain distribution is similar, whereas for high values of  $h$  the mechanical strain gradients are smaller compared to small pyramids. Moreover, the electric field is smaller for bigger pyramid sizes and becomes negligible for  $h$  greater than  $200 \mu\text{m}$ . This phenomena is in accordance with the size effect of flexoelectricity. It is evident that the results of the quadratic element and [16,35] are in good agreement.

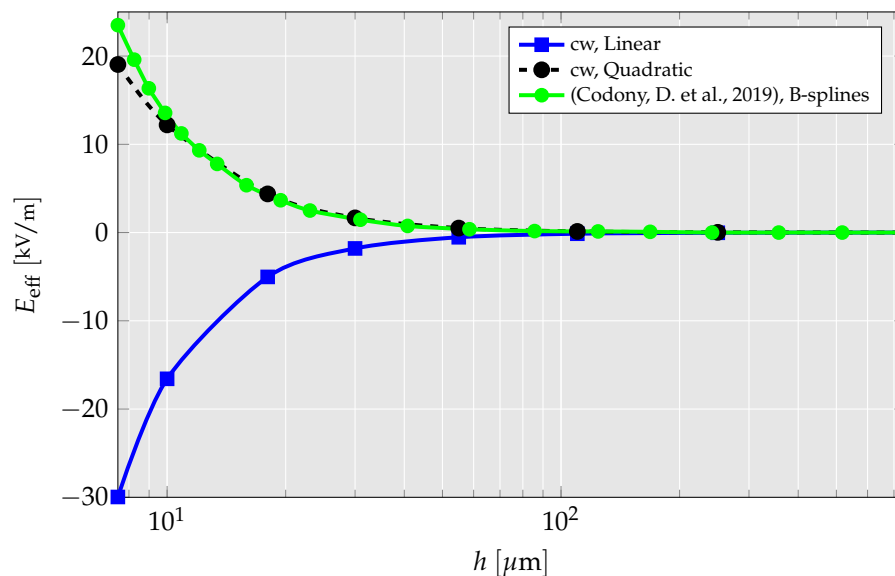


**Figure 31.** Effective electric field  $E_{\text{eff}}$  of the truncated pyramid for linear element, quadratic element and [16] for different geometric sizes.

## 5. Conclusions

In the manuscript, a second-order collocation-based mixed FEM (CMFEM) for flexoelectricity is established. First, CMFEM formulation for linear elements is presented and tested. Because first-order CMFEM has deficiencies and cannot realistically capture flexoelectric material behavior, a quadratic CMFEM element is proposed and implemented. Here, quadratic shape functions are used for the DOFs and, consequently, independent mechanical strains and electric field are assumed to be quadratic polynomials for the collo-

cation. The new elements are implemented as Fortran user elements and tested on several boundary value problems.

The achieved results and drawn conclusions can be summarized as follows.

- A linear CMFEM element is developed and verified with numerical results for a 2D cantilever beam problem from the literature.
- The correctness of the newly proposed quadratic element is verified through comparison with the linear element and examples from the literature. To make the closest comparison, the strain gradient components, which cannot be computed by the linear element, are hardcoded to zero in the quadratic UEL.
- Based on a convergence study, it is shown that the quadratic element is more accurate than the linear element. In particular, for meshes with very few elements, the accuracy is drastically improved with the usage of the newly developed quadratic element.
- By no longer hardcoding specific strain gradient components to zero in the quadratic UEL, CMFEM elements' performance is analyzed. There, it is presented that mechanical strain gradient  $\eta_{333}$  cannot be captured by the linear element, but has a relevant magnitude, leading to a strong overestimation of flexoelectric coupling and mechanical stiffness.
- The abovementioned findings are further investigated by a parameter study in which cantilever beam's deflection and generated electric field are studied for a wide range of flexoelectric coefficients. There, it is found that using the linear element, the cantilever beams' deflection nears zero for high flexoelectric coefficients and the remaining deflection is build-up only from shear stress. For the quadratic element, on the other hand, the deflection saturates at a nonzero value mimicking a physically realistic behavior.
- In the flexoelectric truncated pyramid example, although the linear element produced physically invalid results, the results of the quadratic element are in a very good agreement with the literature. The newly proposed quadratic element yields realistic results compared to those obtained in experiments [8,34] and a distribution of the electric field similar to [12,16]. This is additionally outlined in a simulation series wherein the flexoelectric size effect is visualized.

By using the newly developed second-order formulation, it is possible to model flexoelectric behavior accurately with less computational cost than traditional mixed FEM. This opens the possibility to apply the proposed quadratic element to the computationally demanding nonlinear electromechanical problems. It should be mentioned that there is scope for further improvement by ensuring  $C^1$ -continuity.

**Author Contributions:** Conceptualization, S.K.; methodology, K.T. and P.H.S.; software, K.T.; verification, K.T., P.H.S. and S.K.; formal analysis, K.T., P.H.S. and S.K.; investigation, K.T.; data curation, K.T. and P.H.S.; writing—original draft preparation, K.T.; writing—review and editing, P.H.S. and S.K.; supervision, S.K.; project administration and funding acquisition, S.K. All authors have read and agreed to the published version of the manuscript.

**Funding:** This research was funded by DFG (German Research Foundation) under grant KO 6356/1 "FLEXFRA: Modeling of Flexoelectricity (Strain and Polarization Gradients in Piezo- and Ferroelectric Materials), with Emphasis on Fracture".

**Data Availability Statement:** The source code together with the data that support the findings of this study are available from the corresponding author upon reasonable request.

**Conflicts of Interest:** The authors declare no conflict of interest.

## Abbreviations

The following abbreviations are used in this manuscript:

BVP	boundary value problem
CMFEM	collocation-based mixed finite element method
cw	current work
FEM	finite element method
MEMS	microelectromechanical systems
SGE	strain gradient elasticity
UEL	user element

## References

- Mashkevich, V.; Tolpygo, K. Electrical, optical and elastic properties of diamond type crystals. *Sov. Phys. JETP* **1957**, *5*, 435–439.
- Kogan, S.M. Piezoelectric effect during inhomogeneous deformation and acoustic scattering of carriers in crystals. *Sov. Phys. Solid State* **1964**, *5*, 2069–2070.
- Zubko, P.; Catalan, G.; Tagantsev, A.K. Flexoelectric effect in solids. *Annu. Rev. Mater. Res.* **2013**, *43*, 387–421. [[CrossRef](#)]
- Kozinov, S.; Kuna, M. Simulation of fatigue damage in ferroelectric polycrystals under mechanical/electrical loading. *J. Mech. Phys. Solids* **2018**, *116*, 150–170. [[CrossRef](#)]
- Catalan, G.; Sinnamon, L.; Gregg, J. The effect of flexoelectricity on the dielectric properties of inhomogeneously strained ferroelectric thin films. *J. Phys. Condens. Matter* **2004**, *16*, 2253. [[CrossRef](#)]
- Ma, W.; Cross, L.E. Large flexoelectric polarization in ceramic lead magnesium niobate. *Appl. Phys. Lett.* **2001**, *79*, 4420–4422. [[CrossRef](#)]
- Ma, W.; Cross, L.E. Flexoelectric polarization of barium strontium titanate in the paraelectric state. *Appl. Phys. Lett.* **2002**, *81*, 3440–3442. [[CrossRef](#)]
- Cross, L.E. Flexoelectric effects: Charge separation in insulating solids subjected to elastic strain gradients. *J. Mater. Sci.* **2006**, *41*, 53–63. [[CrossRef](#)]
- Catalan, G.; Lubk, A.; Vlooswijk, A.; Snoeck, E.; Magen, C.; Janssens, A.; Rispens, G.; Rijnders, G.; Blank, D.H.; Noheda, B. Flexoelectric rotation of polarization in ferroelectric thin films. *Nat. Mater.* **2011**, *10*, 963–967. [[CrossRef](#)]
- Hu, S.; Shen, S. Electric field gradient theory with surface effect for nano-dielectrics. *Comput. Mater. Contin.* **2009**, *13*, 63. [[CrossRef](#)]
- Xu, L.; Shen, S. Size-dependent piezoelectricity and elasticity due to the electric field-strain gradient coupling and strain gradient elasticity. *Int. J. Appl. Mech.* **2013**, *5*, 1350015. [[CrossRef](#)]
- Abdollahi, A.; Peco, C.; Millan, D.; Arroyo, M.; Arias, I. Computational evaluation of the flexoelectric effect in dielectric solids. *J. Appl. Phys.* **2014**, *116*, 093502. [[CrossRef](#)]
- Thai, T.Q.; Rabczuk, T.; Zhuang, X. A large deformation isogeometric approach for flexoelectricity and soft materials. *Comput. Methods Appl. Mech. Eng.* **2018**, *341*, 718–739. [[CrossRef](#)]
- Liu, C.; Wang, J.; Xu, G.; Kamlah, M.; Zhang, T.Y. An isogeometric approach to flexoelectric effect in ferroelectric materials. *Int. J. Solids Struct.* **2019**, *162*, 198–210. [[CrossRef](#)]
- Sladek, J.; Stanak, P.; Han, Z.; Sladek, V.; Atluri, S. Applications of the MLPG method in engineering & sciences: A review. *CMES Comput. Model. Eng. Sci.* **2013**, *92*, 423–475. [[CrossRef](#)]
- Codony, D.; Marco, O.; Fernández-Méndez, S.; Arias, I. An immersed boundary hierarchical B-spline method for flexoelectricity. *Comput. Methods Appl. Mech. Eng.* **2019**, *354*, 750–782. [[CrossRef](#)]
- Mao, S.; Purohit, P.K.; Aravas, N. Mixed finite-element formulations in piezoelectricity and flexoelectricity. *Proc. R. Soc. Math. Phys. Eng. Sci.* **2016**, *472*, 20150879. [[CrossRef](#)]
- Sladek, J.; Sladek, V.; Wünsche, M.; Zhang, C. Effects of electric field and strain gradients on cracks in piezoelectric solids. *Eur. J. Mech. A Solids* **2018**, *71*, 187–198. [[CrossRef](#)]
- Deng, F.; Deng, Q.; Yu, W.; Shen, S. Mixed finite elements for flexoelectric solids. *J. Appl. Mech.* **2017**, *84*, 081004. [[CrossRef](#)]
- Serrao, P.H.; Kozinov, S. Numerically robust  $C^0$ -continuous mixed FE for analyses of size-dependent flexoelectricity in piezoelectric solids. **2023**, *submitted*.
- Boffi, D.; Brezzi, F.; Fortin, M. *Mixed Finite Element Methods and Applications*; Springer: Berlin/Heidelberg, Germany, 2013. Volume 44. [[CrossRef](#)]
- Dong, L.; Atluri, S. A simple procedure to develop efficient & stable hybrid/mixed elements, and Voronoi cell finite elements for macro-& micromechanics. *Comput. Mater. Contin.* **2011**, *24*, 61. [[CrossRef](#)]
- Bishay, P.L.; Sladek, J.; Sladek, V.; Atluri, S.N. Analysis of functionally graded magneto-electro-elastic composites using hybrid/mixed finite elements and node-wise material properties. *Comput. Mater. Contin.* **2012**, *29*, 213. [[CrossRef](#)]
- Bishay, P.L.; Atluri, S.N. High-performance 3D hybrid/mixed, and simple 3D Voronoi cell finite elements, for macro-& micro-mechanical modeling of solids, without using multi-field variational principles. *Comput. Model. Eng. Sci.* **2012**, *84*, 41–97.
- Tian, X.; Sladek, J.; Sladek, V.; Deng, Q.; Li, Q. A collocation mixed finite element method for the analysis of flexoelectric solids. *Int. J. Solids Struct.* **2021**, *217*, 27–39. [[CrossRef](#)]

26. Sladek, J.; Sladek, V.; Repka, M.; Pan, E. Size effect in piezoelectric semiconductor nanostructures. *J. Intell. Mater. Syst. Struct.* **2022**, *33*, 1351–1363. [[CrossRef](#)]
27. Nanthakumar, S.; Zhuang, X.; Park, H.S.; Rabczuk, T. Topology optimization of flexoelectric structures. *J. Mech. Phys. Solids* **2017**, *105*, 217–234. [[CrossRef](#)]
28. Gitman, I.M.; Askes, H.; Kuhl, E.; Aifantis, E.C. Stress concentrations in fractured compact bone simulated with a special class of anisotropic gradient elasticity. *Int. J. Solids Struct.* **2010**, *47*, 1099–1107. [[CrossRef](#)]
29. Auld, B.A. *Acoustic Fields and Waves in Solids*; John Wiley and Sons: New York, NY, USA, 1973; pp. 357–382.
30. Shu, L.; Wei, X.; Pang, T.; Yao, X.; Wang, C. Symmetry of flexoelectric coefficients in crystalline medium. *J. Appl. Phys.* **2011**, *110*, 104106. [[CrossRef](#)]
31. Reddaiah, P. Deriving shape functions for 9-noded rectangular element by using lagrange functions in natural coordinate system and verified. *Int. J. Math. Trends Technol.* **2017**, *51*, 429–433. [[CrossRef](#)]
32. Ventura, J.; Codony, D.; Fernández-Méndez, S. A  $C^0$  interior penalty finite element method for flexoelectricity. *J. Sci. Comput.* **2021**, *88*, 1–24. [[CrossRef](#)]
33. Zhuang, X.; Nguyen, B.H.; Nanthakumar, S.S.; Tran, T.Q.; Alajlan, N.; Rabczuk, T. Computational modeling of flexoelectricity—a review. *Energies* **2020**, *13*, 1326. [[CrossRef](#)]
34. Majdoub, M.; Sharma, P.; Çağın, T. Dramatic enhancement in energy harvesting for a narrow range of dimensions in piezoelectric nanostructures. *Phys. Rev. B* **2008**, *78*, 121407. [[CrossRef](#)]
35. Codony, D. Mathematical and Computational Modeling of Flexoelectricity at Mesoscopic and Atomistic Scales. Ph.D. Thesis, Universitat Politècnica de Catalunya, Barcelona, Spain, 2021. Available online: <http://hdl.handle.net/2117/347914> (accessed on 21 December 2022).
36. Hamdia, K.M.; Ghasemi, H.; Zhuang, X.; Alajlan, N.; Rabczuk, T. Computational machine learning representation for the flexoelectricity effect in truncated pyramid structures. *Comput. Mater. Contin.* **2019**, *59*, 79–87. [[CrossRef](#)]

**Disclaimer/Publisher’s Note:** The statements, opinions and data contained in all publications are solely those of the individual author(s) and contributor(s) and not of MDPI and/or the editor(s). MDPI and/or the editor(s) disclaim responsibility for any injury to people or property resulting from any ideas, methods, instructions or products referred to in the content.